Supplement of Atmos. Chem. Phys., 20, 14005–14021, 2020
https://doi.org/10.5194/acp-20-14005-2020-supplement

Atmospheric Chemistry and Physics
Open Access

Supplement of

Is the near-spherical shape the "new black" for smoke?

Anna Gialitaki et al.

Correspondence to: Anna Gialitaki (togialitaki@noa.gr)

Table S1. The retrieved microphysical properties of near-spherical particles, along with their Particle Linear Depolarization Ratio (PLDR) and Lidar Ratio (LR) values at 355, 532 and 1064 nm, that reproduce the PLDR and LR reported in Haarig et al., (2017). Also shown is the corresponding cost function of each solution. The solution that minimizes the cost function (Eq. 8 in the manuscript) is highlighted in blue.

Measurements – Leipzig (22 August 2017)										
				$PLDR_{355}$	$PLDR_{532}$	$PLDR_{1064}$	LR_{355}	LR_{532}	LR_{1064}	
				22.4 ± 1.5	41 ± 16	18.4 ± 0.6	66 ± 12	4.3 ± 0.7	92 ± 27	
Simulations – Near-Spherical particles										
r_g	ε_s	mri	mrr	$PLDR_{355}$	$PLDR_{532}$	$PLDR_{1064}$	LR_{355}	LR_{532}	LR_{1064}	Cost function
0.45	1.1	0.005	1.35	23.189	17.733	2.082	33.032	67.368	118.959	2.538
0.50	1.1	0.005	1.35	23.853	19.529	2.800	29.078	56.023	121.761	4.020
0.35	1.2	0.020	1.45	23.205	17.223	3.894	43.144	62.774	106.101	1.480
0.35	1.2	0.025	1.45	23.104	17.290	3.855	54.299	75.096	117.685	3.250
0.30	1.3	0.025	1.50	22.207	18.081	4.901	43.173	62.971	104.923	0.477
0.30	1.3	0.030	1.50	22.349	18.306	4.846	52.548	73.395	114.380	1.745
0.25	1.4	0.020	1.55	21.152	17.871	4.861	33.992	55.011	90.118	1.488
0.25	**1.4**	**0.025**	**1.55**	**21.382**	**18.096**	**4.784**	**40.596**	**62.914**	**96.868**	**0.374**
0.25	1.4	0.030	1.55	21.613	18.309	4.699	48.147	71.642	103.835	0.807

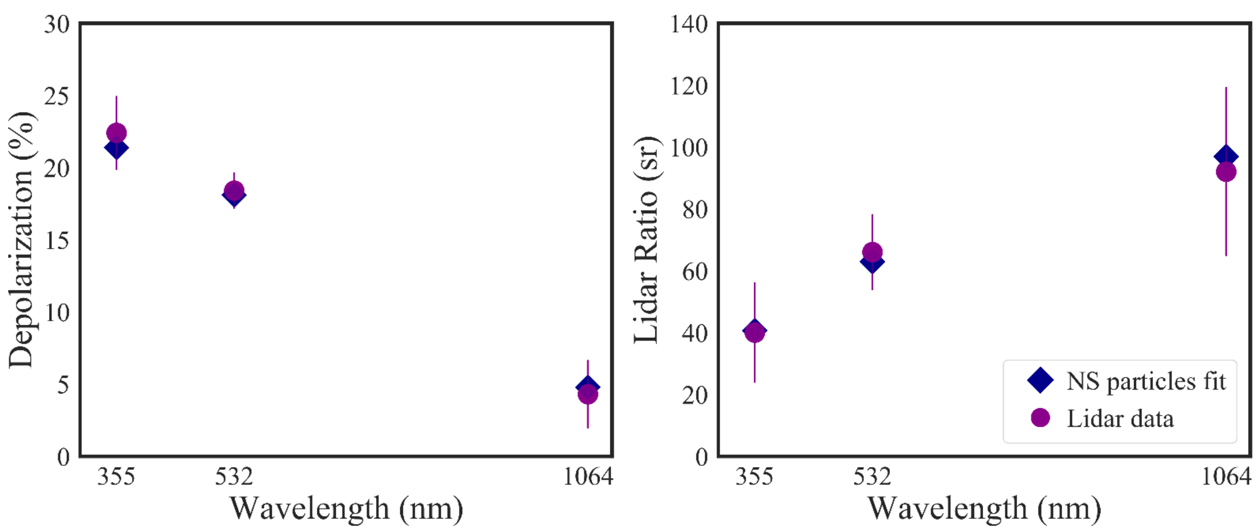

Figure S1. The reproduction of the measured PLDR and LR values, considering near-spherical particles. Purple circles correspond to measurements performed on 22 August 2017, at Leipzig, Germany, while purple lines correspond to the measurement uncertainties. Blue diamonds correspond to simulations performed with the T-matrix code, assuming near-spherical particles, for the values of mean axial ratio ε_s= 1.4, mean geometric radius r_g = 0.25 μm and a wavelength-independent complex refractive index m = 1.55 + i0.025.

Table S2. The retrieved microphysical properties of Chebychev particles of second degree, along with their PLDR and LR values at 355, 532 and 1064 nm, that reproduce the PLDR and LR reported in Haarig et al., (2017). Also shown is the corresponding cost function of each solution. The solution that minimizes the cost function (Eq. 8 in the manuscript) is highlighted in blue.

Simulations – Chebyshev particles of 2nd degree										
r_g	u	mri	mrr	$PLDR_{355}$	$PLDR_{532}$	$PLDR_{1064}$	LR_{355}	LR_{532}	LR_{1064}	Cost function
0.50	-0.05	0.015	1.40	22.589	18.053	3.305	43.954	62.860	114.132	1.078
0.35	-0.10	0.020	1.45	23.941	19.032	4.306	41.378	61.939	105.708	1.037
0.35	-0.10	0.025	1.45	24.182	19.101	4.266	52.324	74.010	117.193	2.760
0.25	-0.20	0.030	1.60	21.472	18.594	6.423	38.733	54.839	94.683	1.897
0.25	-0.20	0.035	1.60	21.442	18.856	6.349	45.443	62.149	101.450	1.426
0.25	-0.20	0.040	1.60	21.435	19.109	6.261	52.956	70.141	108.397	2.368
0.25	0.10	0.045	1.60	22.957	17.647	4.986	45.191	58.417	106.283	1.317
0.25	0.10	0.050	1.60	23.079	17.814	4.932	52.224	65.980	113.890	1.629
0.20	-0.25	0.025	1.65	21.805	19.105	5.129	35.099	55.727	80.981	1.525
0.20	**-0.25**	**0.030**	**1.65**	**21.972**	**19.299**	**5.002**	**40.346**	**61.968**	**85.270**	**0.860**
0.20	-0.25	0.035	1.65	22.135	19.478	4.875	46.274	68.677	89.572	1.092
0.15	0.15	0.050	1.80	24.682	18.822	3.662	38.078	55.301	68.866	2.577
0.15	0.15	0.055	1.80	24.866	18.937	3.589	41.633	59.639	71.027	2.164

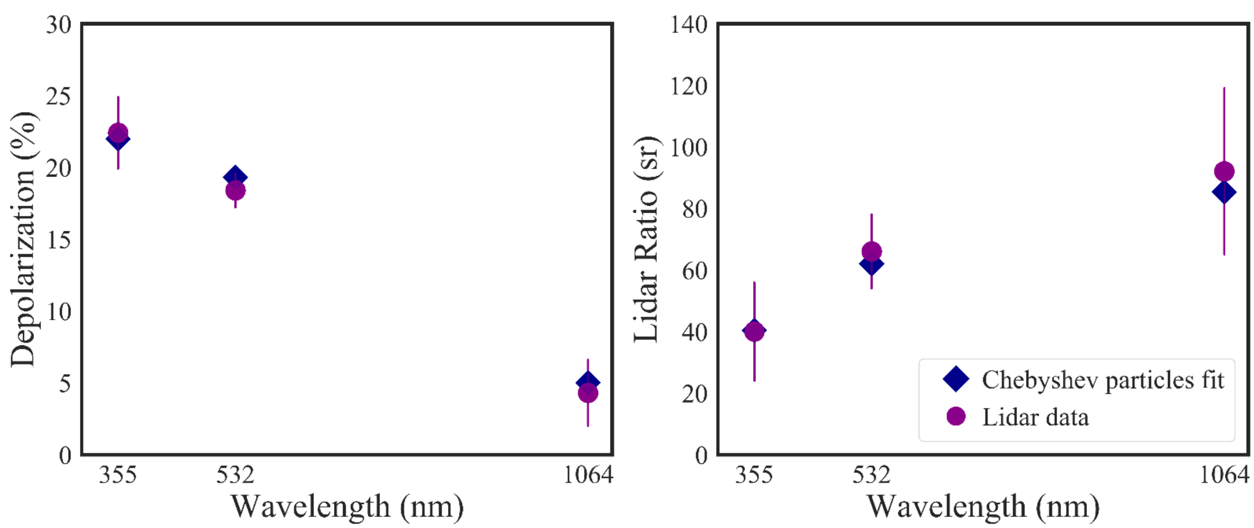

Figure S2. The reproduction of the measured PLDR and LR values, considering Chebyshev particles of second degree. Purple circles correspond to measurements performed on 22 August 2017, at Leipzig, Germany, while purple lines correspond to the measurement uncertainties. Blue diamonds correspond to simulations performed with the T-matrix code, assuming Chebyshev particles of second degree, for the values of deformation parameter u = - 0.25, mean geometric radius r_g = 0.2 μm and a wavelength-independent complex refractive index m = 1.65 + i0.03.

Table S3. The retrieved microphysical properties of Chebychev particles of fourth degree, along with their PLDR and LR values at 355, 532 and 1064 nm, that reproduce the PLDR and LR reported in Haarig et al., (2017). Only one solution was found.

Simulations – Chebyshev particles of 4th degree										
r_g	u	mri	mrr	$PLDR_{355}$	$PLDR_{532}$	$PLDR_{1064}$	LR_{355}	LR_{532}	LR_{1064}	Cost function
0.55	-0.10	0.01	1.35	23.021	17.729	5.072	44.133	67.510	122.244	1.824

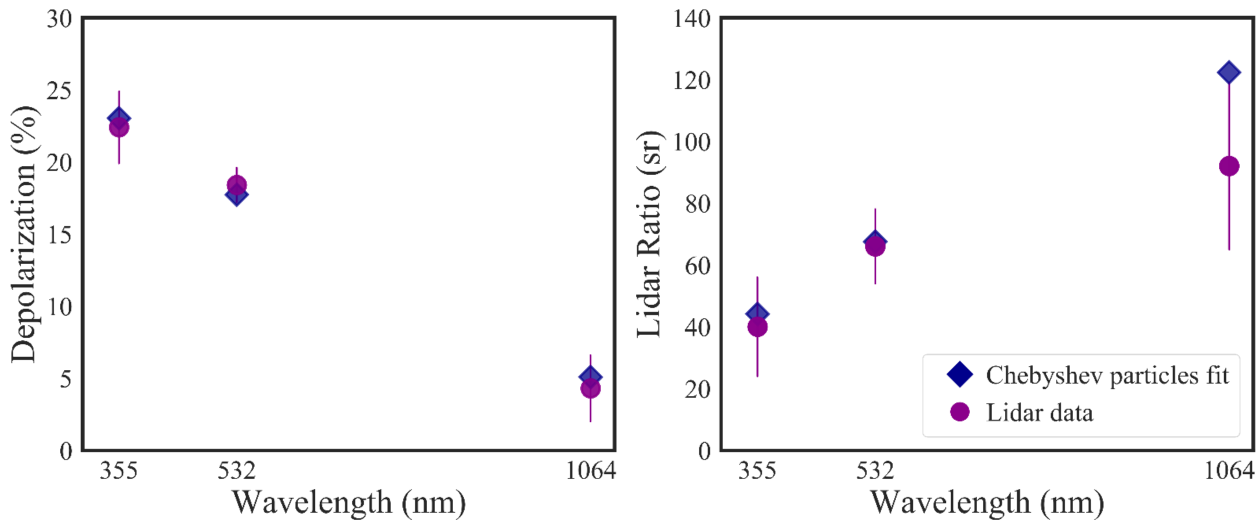

Figure S3. The reproduction of the measured PLDR and LR values, considering Chebyshev particles of fourth degree. Purple circles correspond to measurements performed on 22 August 2017, at Leipzig, Germany, while purple lines correspond to the measurement uncertainties. Blue diamonds correspond to simulations performed with the T-matrix code, assuming Chebyshev particles of fourth degree, for the values of deformation parameter u = - 0.1, mean geometric radius r_g = 0.55 μm and a wavelength-independent complex refractive index m = 1.35 + i0.01.

Table S4. The retrieved microphysical properties of near-spherical particles calculated, along with their PLDR and LR values at 355, 532 and 1064 nm, that reproduce the PLDR and LR reported in Hu et al., (2019). Also shown is the corresponding cost function of each solution. The solution that minimizes the cost function (Eq. 8 in the manuscript) is highlighted in blue.

				Measurements – Lille (31 August 2017)					
				$PLDR_{355}$	$PLDR_{532}$	$PLDR_{1064}$	LR_{355}	LR_{532}	
				28 ± 8	18 ± 3	5 ± 1	34 ± 12	58 ± 20	
				Simulations – Near-spherical particles					
r_g	ε_s	mri	mrr	$PLDR_{355}$	$PLDR_{532}$	$PLDR_{1064}$	LR_{355}	LR_{532}	Cost function
0.30	1.3	0.005	1.45	27.224	20.388	4.185	23.699	45.371	2.442
0.30	1.3	0.010	1.45	27.634	20.564	4.111	30.216	54.191	1.659
0.35	1.25	0.010	1.45	26.360	20.903	5.267	25.340	42.825	2.146
0.30	1.3	0.015	1.45	27.986	20.706	4.039	38.032	64.250	1.949
0.40	0.9	0.015	1.45	29.210	18.796	4.165	33.582	43.511	1.316
0.40	1.2	0.015	1.45	24.525	19.552	5.597	31.282	44.263	1.336
0.45	1.15	0.015	1.45	21.853	16.377	4.955	32.896	40.472	1.662
0.40	0.9	0.020	1.45	28.275	18.615	4.158	43.032	53.082	1.379
0.40	1.2	0.020	1.45	24.287	19.630	5.588	40.723	54.218	1.206
0.45	1.15	0.020	1.45	21.089	16.281	4.996	43.488	50.209	1.851
0.25	1.4	0.005	1.50	25.199	18.971	4.015	24.969	47.048	2.064
0.25	1.45	0.005	1.50	27.020	20.875	4.465	26.132	49.425	1.833
0.30	1.3	0.010	1.50	21.788	17.318	5.036	22.590	38.351	2.525
0.30	1.35	0.010	1.50	24.343	20.213	5.999	23.333	40.266	3.329
0.30	1.3	0.015	1.50	21.919	17.584	4.993	28.331	45.535	1.209
0.30	1.35	0.015	1.50	24.536	20.495	5.944	29.195	47.680	2.197
0.30	0.85	0.020	1.50	26.909	18.516	4.481	29.638	44.079	0.934
0.30	1.3	0.020	1.50	22.062	17.841	4.949	35.150	53.709	0.611
0.30	1.35	0.020	1.50	24.730	20.764	5.878	36.151	56.088	1.829
0.30	**0.85**	**0.025**	**1.50**	**26.865**	**18.643**	**4.438**	**36.307**	**51.896**	**0.512**
0.30	1.3	0.025	1.50	22.207	18.081	4.901	43.173	62.971	1.181
0.30	0.85	0.030	1.50	26.807	18.760	4.396	44.115	60.795	1.181
0.25	1.4	0.010	1.55	20.723	17.457	5.009	23.291	41.498	2.338
0.25	1.45	0.010	1.55	22.701	19.475	5.614	24.449	43.734	2.199
0.25	1.4	0.015	1.55	20.927	17.658	4.936	28.252	47.887	1.284
0.25	1.45	0.015	1.55	22.919	19.674	5.522	29.599	50.361	1.267

0.25	1.5	0.015	1.55	24.1923	20.997	5.914	30.589	52.070	2.228
0.25	1.4	0.020	1.55	21.1515	17.871	4.861	33.992	55.011	0.776
0.25	1.45	0.02	1.55	23.1466	19.885	5.422	35.550	57.725	0.957
0.25	1.4	0.025	1.55	21.3824	18.096	4.784	40.596	62.914	1.094

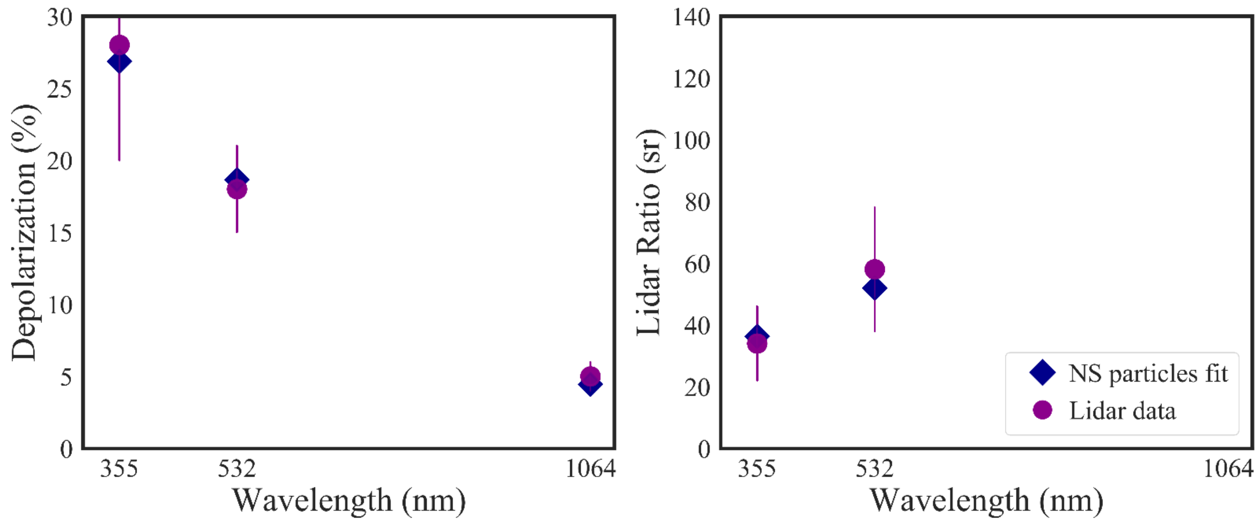

Figure S4. The reproduction of the measured PLDR and LR values, considering near-spherical particles. Purple circles correspond to measurements performed on 31 August 2017, at Lille, France, while purple lines correspond to the measurement uncertainties. Blue diamonds correspond to simulations performed with the T-matrix code, assuming near-spherical particles, for the values of mean axial ratio ε_s = 0.85, mean geometric radius r_g = 0.3 μm and a wavelength-independent complex refractive index m = 1.5 + i0.025.

Table S5. The retrieved microphysical properties of Chebyshev particles of second degree calculated, along with their PLDR and LR values at 355, 532 and 1064 nm, that reproduce the PLDR and LR reported in Hu et al., (2019). Also shown is the corresponding cost function of each solution. The solution that minimizes the cost function (Eq. 8 in the manuscript) is highlighted in blue.

Simulations-Chebyshev particles of 2nd degree									
r_g	u	mri	mrr	$PLDR_{355}$	$PLDR_{532}$	$PLDR_{1064}$	LR_{355}	LR_{532}	Cost function
0.35	-0.10	0.010	1.45	23.088	18.892	4.371	24.778	42.457	2.056
0.35	-0.10	0.015	1.45	23.587	18.972	4.341	32.265	51.481	0.971
0.45	0.05	0.015	1.45	28.904	19.053	4.180	30.416	39.669	1.737
0.35	-0.10	0.020	1.45	23.941	19.032	4.306	41.378	61.939	1.274
0.45	0.05	0.020	1.45	27.796	18.656	4.181	40.472	49.009	1.212
0.30	-0.15	0.010	1.50	25.802	20.113	5.662	23.156	38.673	2.760
0.30	-0.15	0.015	1.50	25.676	20.321	5.616	28.859	45.770	1.620
0.30	-0.15	0.020	1.50	25.636	20.526	5.564	35.627	53.846	1.177
0.30	-0.15	0.025	1.50	25.638	20.726	5.474	43.599	62.987	1.839
0.25	-0.20	0.010	1.55	25.375	20.627	5.594	24.156	41.421	2.588
0.25	-0.20	0.015	1.55	25.634	20.807	5.511	29.168	47.788	1.647
0.25	-0.20	0.020	1.55	25.870	20.992	5.423	34.951	54.871	1.275
0.25	0.10	0.020	1.55	27.876	19.180	4.447	24.013	40.215	1.944
0.25	0.10	0.025	1.55	28.029	19.338	4.391	28.927	46.368	1.086
0.25	0.10	0.030	1.55	28.167	19.492	4.332	34.570	53.246	0.753
0.25	0.10	0.035	1.55	28.284	19.639	4.269	41.014	60.899	1.197
0.20	-0.25	0.005	1.60	27.733	19.926	4.443	23.233	43.627	2.045
0.20	-0.25	0.010	1.60	27.621	20.033	4.322	27.397	49.241	1.416
0.20	-0.25	0.015	1.60	27.532	20.138	4.203	32.218	55.355	1.186
0.20	-0.25	0.020	1.60	27.490	20.232	4.085	37.560	61.989	1.523
0.25	0.10	0.030	1.60	22.380	17.091	5.129	28.331	39.668	1.665
0.25	0.10	0.035	1.60	22.604	17.281	5.094	33.291	45.295	0.928
0.25	**0.10**	**0.040**	**1.60**	**22.797**	**17.468**	**5.033**	**38.894**	**51.532**	**0.726**
0.25	0.10	0.045	1.60	22.957	17.647	4.985	45.191	58.417	1.282
0.20	-0.25	0.010	1.65	21.578	18.405	5.497	22.049	39.853	2.724
0.20	-0.25	0.015	1.65	21.616	18.640	5.378	25.879	44.770	1.721
0.20	-0.25	0.020	1.65	21.673	18.854	5.256	30.279	50.091	1.024
0.20	-0.25	0.025	1.65	21.805	19.105	5.129	35.099	55.727	0.773
0.20	-0.25	0.030	1.65	21.972	19.299	5.002	40.346	61.968	1.074

0.15	0.15	0.040	1.85	23.577	18.201	4.460	28.149	40.754		1.583
0.15	0.15	0.045	1.85	23.691	18.323	4.386	30.838	44.033		1.236
0.15	0.15	0.050	1.85	23.796	18.438	4.310	33.703	47.494		1.050
0.15	0.15	0.055	1.85	23.887	18.544	4.234	36.750	51.131		1.054

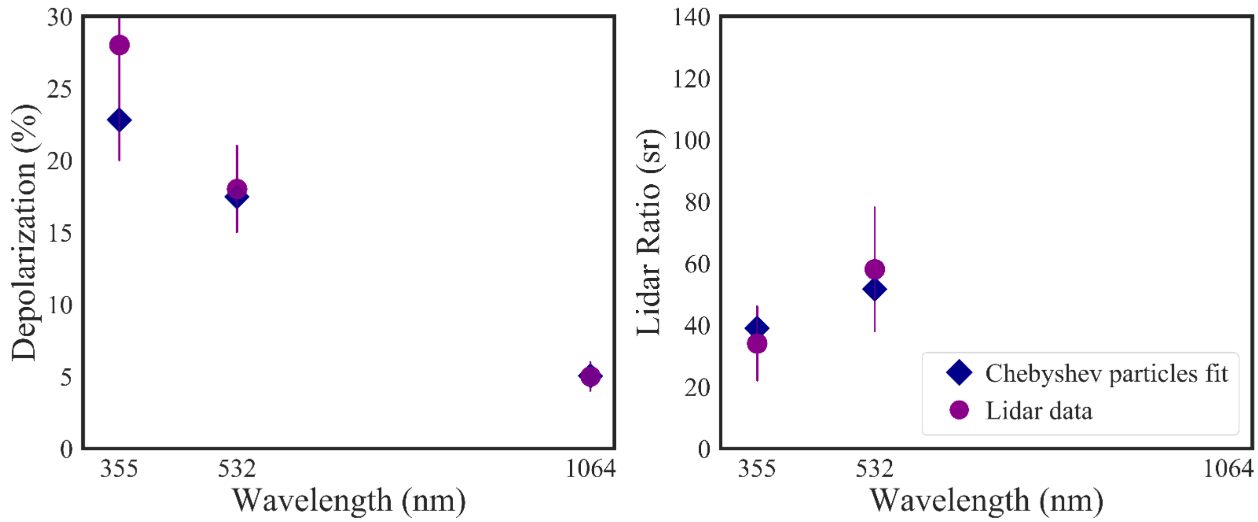

Figure S5. The reproduction of the measured PLDR and LR values, considering Chebyshev particles of second degree. Purple circles correspond to measurements performed on 31 August 2017, at Lille, France, while purple lines correspond to the measurement uncertainties. Blue diamonds correspond to simulations performed with the T-matrix code, assuming Chebyshev particles of second degree, for the values of deformation parameter u = 0.1, mean geometric radius r_g = 0.25 μm and a wavelength-independent complex refractive index m = 1.6 + i0.04.

Table S6. The retrieved microphysical properties of Chebyshev particles of fourth degree, along with their PLDR and LR values at 355, 532 and 1064 nm, that reproduce the PLDR and LR reported in Hu et al., (2019). Also shown is the corresponding cost function of each solution. The solution that minimizes the cost function (Eq. 8 in the manuscript) is highlighted in blue.

Simulations-Chebyshev particles of 4th degree									
r_g	u	mri	mrr	$PLDR_{355}$	$PLDR_{532}$	$PLDR_{1064}$	LR_{355}	LR_{532}	Cost function
0.50	-0.10	0.005	1.35	22.271	16.441	4.236	31.222	56.123	1.429
0.55	-0.10	0.005	1.35	23.105	17.572	5.082	28.315	50.004	0.786
0.55	-0.10	0.010	1.35	23.021	17.729	5.072	44.133	67.510	1.340
0.40	0.10	0.015	1.45	27.938	18.477	4.592	25.960	39.366	1.509
0.40	**0.10**	**0.020**	**1.45**	**27.387**	**18.480**	**4.551**	**34.838**	**49.319**	**0.426**
0.40	0.10	0.025	1.50	21.128	15.107	4.969	34.601	42.152	2.230
0.40	0.10	0.030	1.50	20.603	15.108	4.970	45.054	51.563	2.737

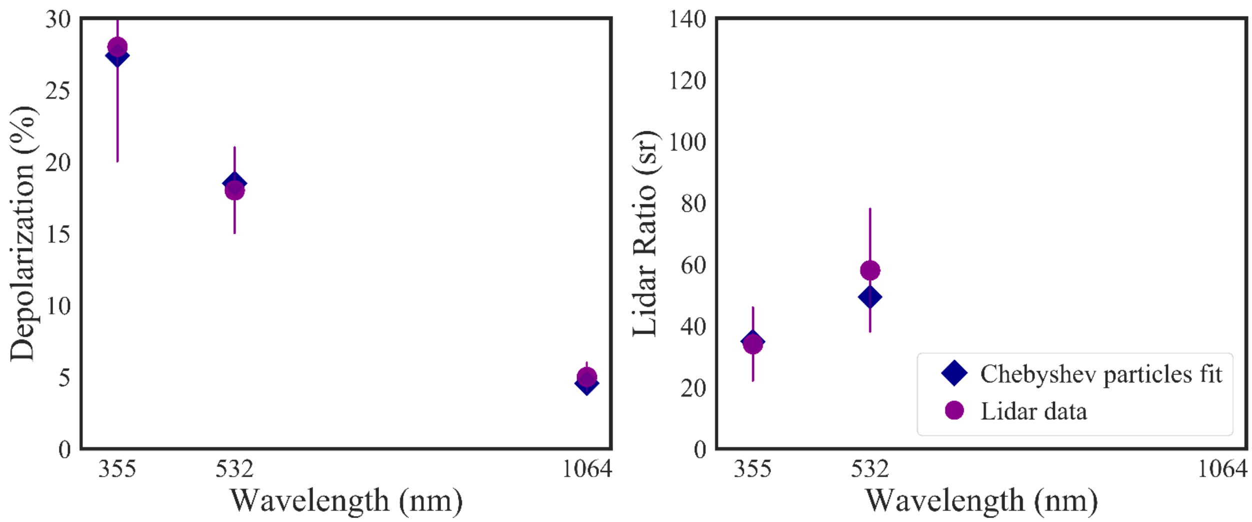

Figure S6. The reproduction of the measured PLDR and LR values, considering Chebyshev particles of fourth degree. Purple circles correspond to measurements performed on 31 August 2017, at Lille, France, while purple lines correspond to the measurement uncertainties. Blue diamonds correspond to simulations performed with the T-matrix code, assuming Chebyshev particles of fourth degree, for the values of deformation parameter u = 0.1, mean geometric radius r_g = 0.4 μm and a wavelength-independent complex refractive index m = 1.45 + i0.02.

Table S7. The retrieved microphysical properties of near-spherical particles, along with their PLDR and LR values at 355 and 532 nm, that reproduce the PLDR and LR reported in Ohneiser et al., (2020). Also shown is the corresponding cost function of each solution. The solution that minimizes the cost function (Eq. 8 in the manuscript) is highlighted in blue.

Measurements - Punta Arenas (8 January 2020)								
				$PLDR_{355}$	$PLDR_{532}$	LR_{355}	LR_{532}	
				23 ± 4.6	14 ± 1.4	83 ± 24.9	102 ± 20.4	
				Simulations - Near-spherical particles				
r_g	ε_s	mri	mrr	$PLDR_{355}$	$PLDR_{532}$	LR_{355}	LR_{532}	Cost function
0.45	0.95	0.015	1.35	20.533	14.375	68.950	117.316	1.241
0.25	1.25	0.015	1.40	26.870	12.980	69.944	106.050	1.553
0.25	1.25	0.020	1.40	26.887	12.775	84.989	121.828	2.431
0.40	1.1	0.020	1.40	19.610	12.815	69.217	97.665	1.612
0.45	0.95	0.020	1.40	19.863	13.157	71.215	92.543	1.267
0.45	1.1	0.020	1.40	20.768	15.106	65.201	87.544	1.872
0.50	0.95	0.020	1.40	21.016	15.095	69.684	84.487	1.821
0.40	1.1	0.025	1.40	19.120	12.611	88.727	118.305	2.387
0.45	0.95	0.025	1.40	19.092	12.854	92.073	113.359	1.835
0.45	1.1	0.025	1.40	20.144	14.876	84.954	107.631	0.860
0.50	0.95	0.025	1.40	20.089	14.736	91.343	104.770	0.808
0.20	1.45	0.010	1.45	26.924	13.738	60.070	91.191	1.892
0.20	1.45	0.015	1.45	27.031	13.572	70.695	102.230	1.106
0.20	1.45	0.020	1.45	27.088	13.387	82.625	114.079	1.332
0.25	1.25	0.025	1.45	22.795	12.984	69.706	102.283	0.814
0.30	1.2	0.025	1.45	21.476	14.051	59.836	87.203	1.503
0.25	1.25	0.030	1.45	22.904	12.942	83.346	116.955	1.110
0.30	**1.2**	**0.030**	**1.45**	**21.471**	**14.072**	**73.113**	**101.938**	**0.271**
0.35	0.9	0.030	1.45	24.021	15.237	68.004	86.189	1.793
0.40	1.15	0.030	1.45	18.902	14.573	70.180	81.793	2.208
0.30	1.2	0.035	1.45	21.434	14.080	88.544	118.438	0.818
0.35	0.9	0.035	1.45	23.434	15.134	83.115	101.861	0.665
0.40	1.15	0.035	1.45	18.448	14.545	87.257	97.863	1.201
0.35	0.9	0.040	1.45	22.842	15.015	100.677	119.660	1.780
0.20	1.4	0.020	1.50	23.356	13.602	58.848	89.040	1.431
0.20	1.45	0.020	1.50	25.292	14.966	61.231	92.170	1.721

0.20	1.4	0.025	1.50	23.566	13.579	68.581	99.547	0.456
0.20	1.45	0.025	1.50	25.475	14.904	71.187	102.747	0.933
0.20	1.4	0.030	1.50	23.744	13.533	79.451	110.828	0.345
0.20	1.45	0.030	1.50	25.616	14.815	82.269	114.071	1.013
0.25	1.3	0.030	1.50	21.226	14.888	59.573	87.655	1.931
0.25	0.85	0.035	1.50	23.505	14.616	58.150	85.260	1.875
0.25	1.3	0.035	1.50	21.434	15.009	70.527	99.865	0.897
0.30	1.25	0.035	1.50	19.050	15.175	61.876	82.253	3.099
0.25	0.85	0.040	1.50	23.541	14.661	68.626	97.410	0.621
0.25	1.3	0.040	1.50	21.624	15.097	82.910	113.242	1.007
0.30	1.25	0.040	1.50	19.138	15.352	74.103	95.106	1.879
0.25	0.85	0.045	1.50	23.546	14.690	80.509	110.775	0.452
0.15	0.75	0.030	1.55	27.353	13.055	63.062	90.626	2.303
0.20	1.4	0.030	1.55	20.489	14.088	59.107	88.491	1.661
0.15	0.75	0.035	1.55	27.463	12.938	70.785	98.602	1.785
0.20	1.4	0.035	1.55	20.749	14.162	68.125	98.458	0.640
0.15	0.75	0.040	1.55	27.536	12.818	79.172	106.924	1.767
0.20	1.4	0.040	1.55	20.982	14.213	78.106	109.115	0.376
0.15	0.75	0.045	1.55	27.569	12.678	88.228	115.622	2.368
0.20	1.4	0.045	1.55	21.199	14.237	89.061	120.459	1.060
0.25	0.85	0.050	1.55	18.422	13.365	65.307	88.740	2.124
0.25	0.85	0.055	1.55	18.496	13.476	75.748	100.377	1.190
0.15	0.75	0.040	1.60	27.022	14.633	61.547	91.0133	2.001
0.15	0.75	0.045	1.60	27.182	14.577	68.600	98.7133	1.357
0.15	0.75	0.050	1.60	27.301	14.496	76.214	106.769	1.129
0.15	0.75	0.055	1.60	27.386	14.399	84.395	115.146	1.409
0.15	0.75	0.040	1.55	27.536	12.818	79.172	106.924	1.767

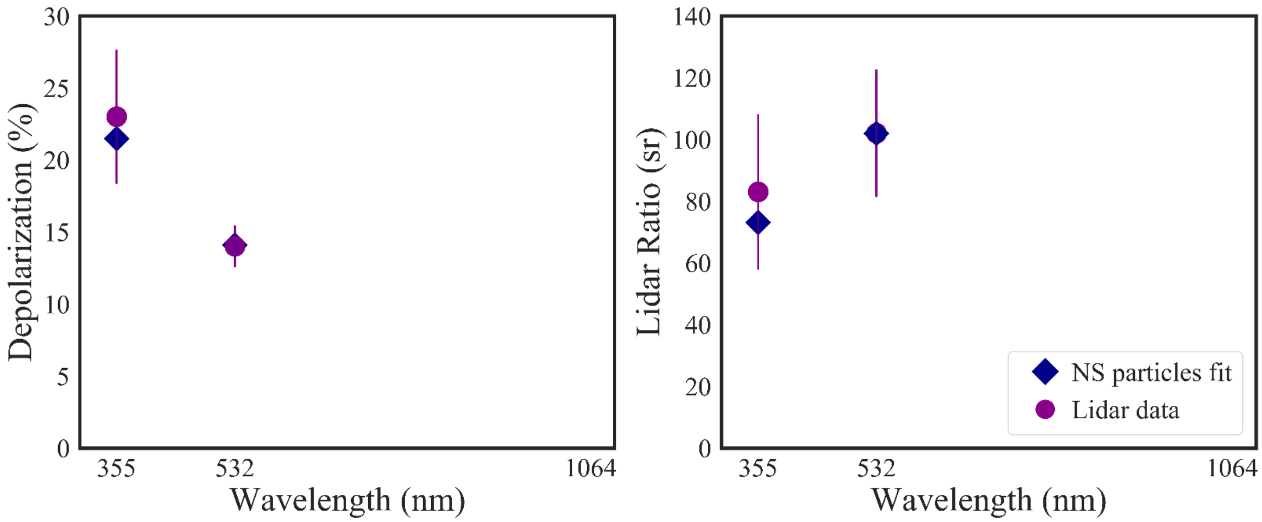

Figure S7. The reproduction of the measured PLDR and LR values, considering near-spherical particles. Purple circles correspond to measurements performed on 8 January 2020, at Punta Arenas, Chile, while purple lines correspond to the measurement uncertainties. Blue diamonds correspond to simulations performed with the T-matrix code, assuming near-spherical particles, for the values of mean axial ratio ε_s = 1.2, mean geometric radius r_g= 0.3 μm and a wavelength-independent complex refractive index m = 1.45 + i0.03.

Table S8. The retrieved microphysical properties of Chebychev particles of the second degree, along with their PLDR and LR values at 355 and 532 nm, that reproduce the PLDR and LR reported in Ohneiser et al., (2020). Also shown is the corresponding cost function of each solution. The solution that minimizes the cost function (Eq. 8 in the manuscript) is highlighted in blue

Simulations-Chebyshev particles of 2nd degree								
r_g	u	mri	mrr	$PLDR_{355}$	$PLDR_{532}$	LR_{355}	LR_{532}	Cost function
0.40	-0.05	0.020	1.40	20.090	13.277	66.484	97.663	1.153
0.40	-0.05	0.025	1.40	19.813	13.047	86.104	118.240	1.59
0.40	0.05	0.035	1.45	22.385	15.166	82.266	95.045	0.828
0.40	0.05	0.040	1.45	21.555	14.941	101.548	112.991	1.395
0.20	0.10	0.030	1.50	27.517	13.750	59.517	90.605	2.198
0.20	0.10	0.035	1.50	27.547	13.692	69.021	101.521	1.341
0.20	0.10	0.040	1.50	27.545	13.606	79.666	113.328	1.381
0.25	-0.15	0.040	1.55	18.754	15.254	60.971	83.462	3.262
0.20	0.10	0.045	1.55	24.027	14.140	65.164	97.931	0.613
0.20	**0.10**	**0.050**	**1.55**	**24.130**	**14.157**	**74.722**	**108.887**	**0.297**
0.20	0.10	0.055	1.55	24.197	14.151	85.247	120.608	0.919
0.15	-0.25	0.025	1.60	23.345	12.886	59.601	87.295	2.041
0.15	-0.25	0.030	1.60	23.395	12.791	67.061	94.899	1.284
0.15	-0.25	0.035	1.60	23.436	12.690	75.143	102.756	0.986
0.20	0.10	0.055	1.60	20.475	13.911	64.504	92.894	1.056
0.15	-0.25	0.035	1.65	20.722	13.836	60.370	88.164	1.545
0.15	-0.25	0.040	1.65	20.953	13.810	67.281	95.492	0.717
0.15	-0.25	0.045	1.65	21.094	13.768	74.976	103.061	0.306
0.15	-0.25	0.050	1.65	21.267	13.673	83.039	111.062	0.394
0.15	-0.25	0.055	1.65	21.397	13.591	91.758	119.209	1.042
0.15	-0.25	0.045	1.70	18.466	14.451	62.057	88.638	2.212
0.15	-0.25	0.050	1.70	18.770	14.460	68.548	95.691	1.386
0.15	-0.25	0.055	1.70	19.045	14.454	75.748	102.914	0.932

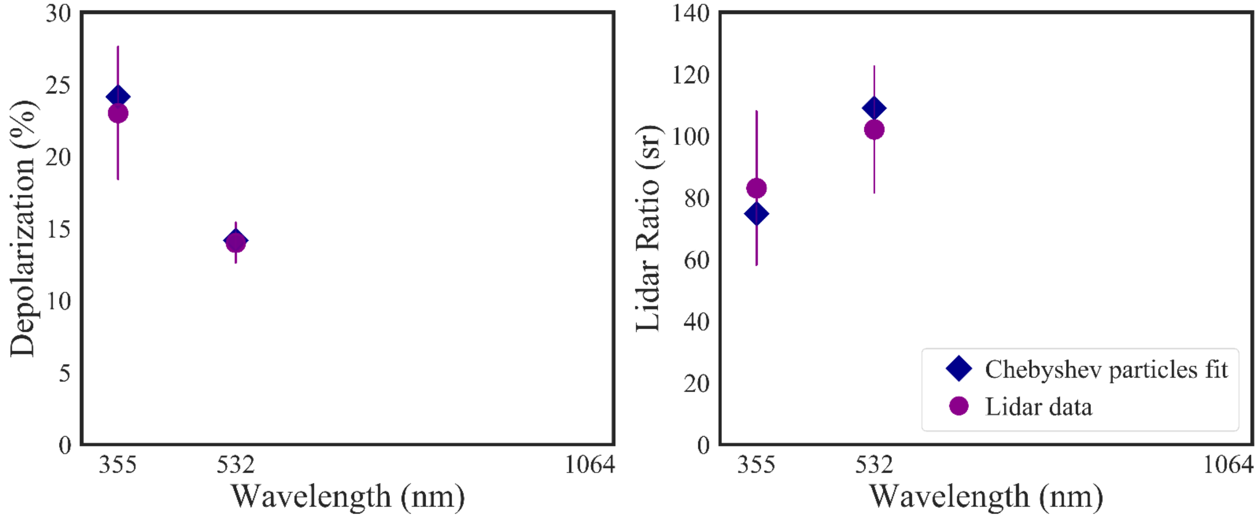

Figure S8. The reproduction of the measured PLDR and LR values, considering Chebyshev particles of second degree. Purple circles correspond to measurements performed on 8 January 2020, at Punta Arenas, Chile, while purple lines correspond to the measurement uncertainties. Blue diamonds correspond to simulations performed with the T-matrix code, assuming Chebyshev particles of second degree, for the values of deformation parameter $u = 0.1$, mean geometric radius $r_g = 0.2$ μm and a wavelength-independent complex refractive index $m = 1.55 + i0.05$.

Table S9. The retrieved microphysical properties of Chebychev particles of the fourth degree, along with their PLDR and LR values at 355 and 532nm, that reproduce the PLDR and LR reported in Ohneiser et al., (2020). Also shown is the corresponding cost function of each solution. The solution that minimizes the cost function (Eq. 8 in the manuscript) is highlighted in blue

Simulations-Chebyshev particles of 4th degree								
r_g	u	mri	mrr	$PLDR_{355}$	$PLDR_{532}$	LR_{355}	LR_{532}	Cost function
0.40	-0.10	0.010	1.35	19.954	12.879	58.858	92.032	2.259
0.40	-0.10	0.015	1.35	19.974	12.941	81.473	114.518	1.385
0.40	0.05	0.015	1.35	24.898	13.684	70.044	122.151	1.468
0.45	-0.10	0.015	1.35	21.261	15.066	74.416	105.070	0.864
0.30	0.10	0.020	1.40	24.960	13.527	64.104	100.577	0.877
0.45	0.05	0.020	1.40	19.388	12.880	60.810	84.889	2.754
0.30	0.10	0.025	1.40	24.878	13.277	81.276	118.818	1.118
0.50	**0.05**	**0.025**	**1.40**	**20.156**	**14.390**	**80.062**	**96.941**	**0.535**
0.50	0.05	0.030	1.40	19.255	13.932	107.122	120.988	2.470
0.35	0.10	0.040	1.50	18.668	13.196	71.794	82.782	2.307
0.40	0.10	0.045	1.50	19.076	15.003	89.782	90.135	1.653

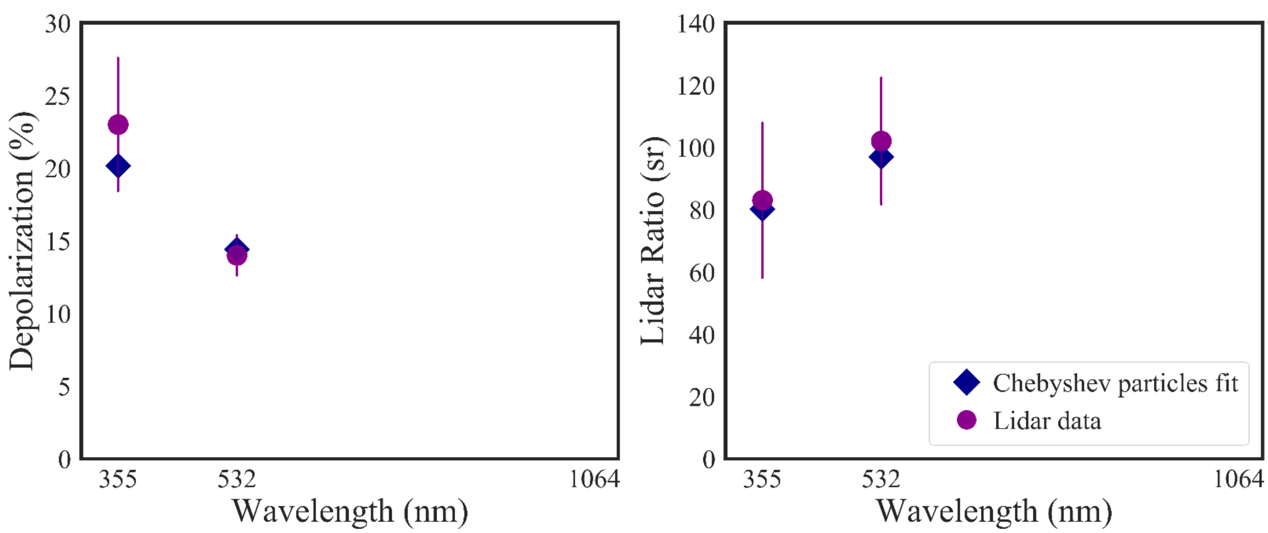

Figure S9. The reproduction of the measured PLDR and LR values, considering Chebyshev particles of fourth degree. Purple circles correspond to measurements performed on 8 January 2020, at Punta Arenas, Chile, while purple lines correspond to the measurement uncertainties. Blue diamonds correspond to simulations performed with the T-matrix code, assuming Chebyshev particles of fourth degree, for the values of deformation parameter u = 0.05, mean geometric radius r_g= 0.5 μm and a wavelength-independent complex refractive index m = 1.4 + i0.025.

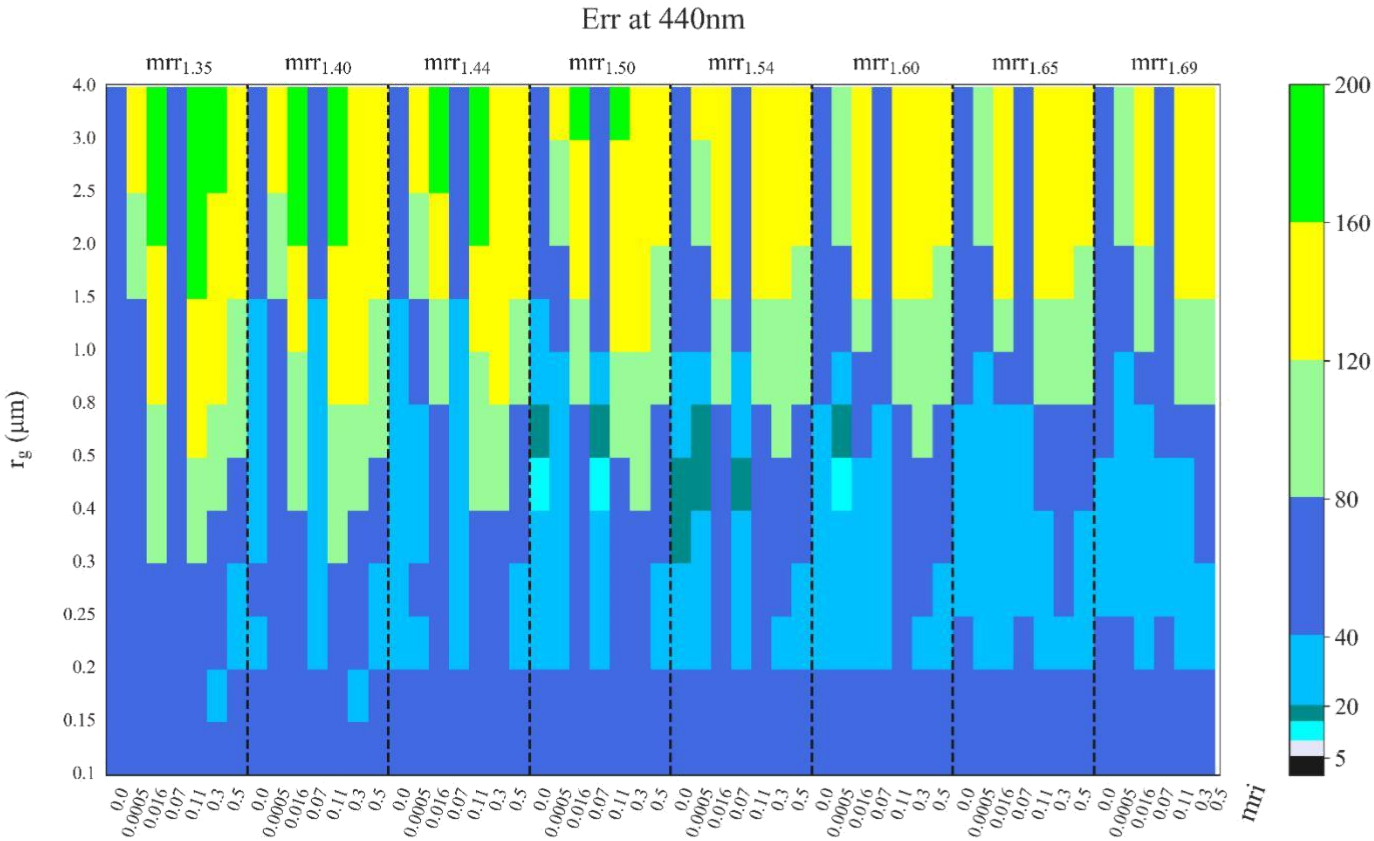

Figure S10. The residual error (Err) of fitting the phase functions at 440 nm of the near-spherical particles presented in the manuscript, with the phase functions calculated with the AERONET non-spherical model, for radius and complex refractive index shown in y- and x-axis, respectively.

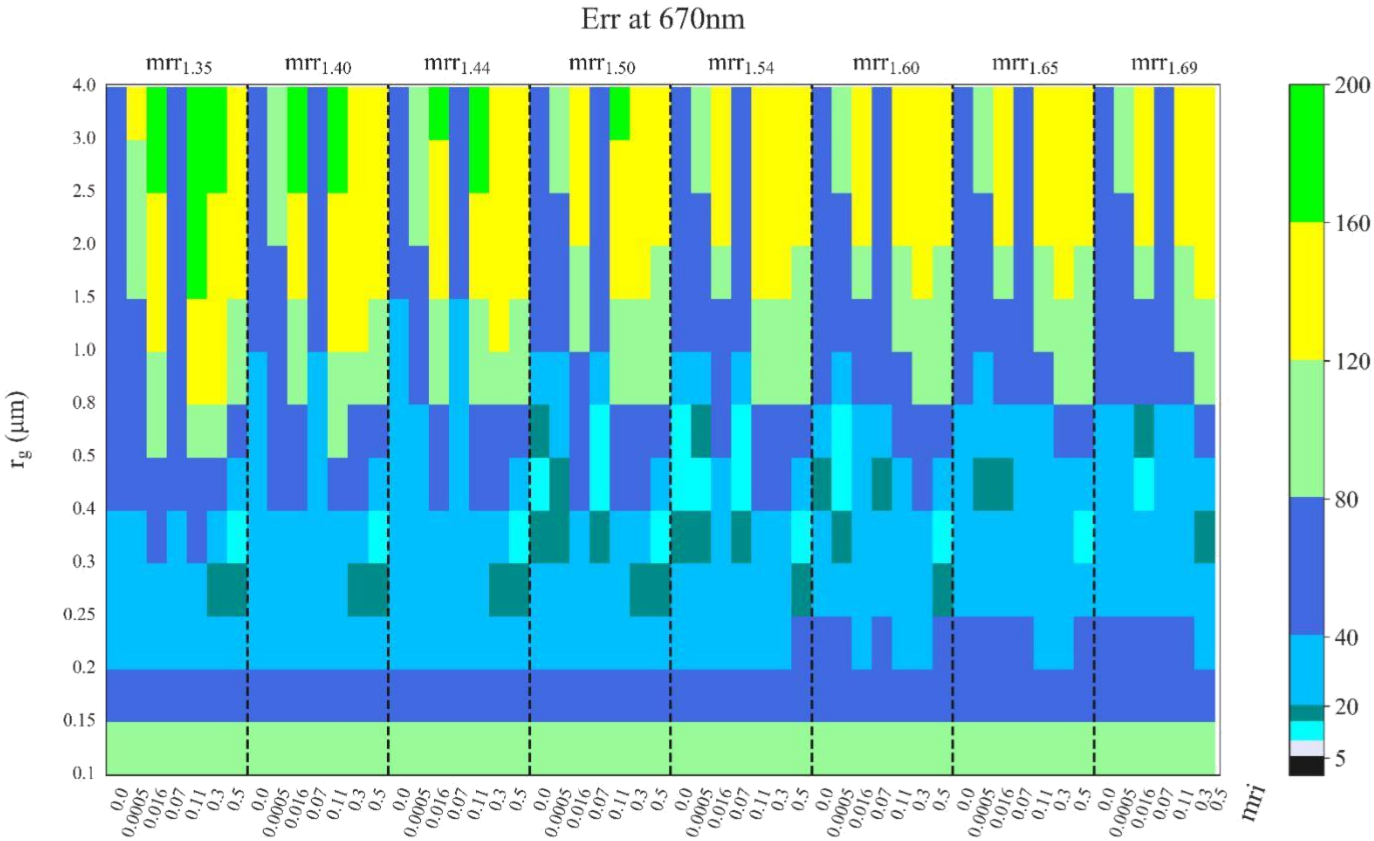

Figure S11. The residual error (Err) of fitting the phase functions at 670 nm of the near-spherical particles presented in the manuscript, with the phase functions calculated with the AERONET non-spherical model, for radius and complex refractive index shown in y- and x-axis, respectively.

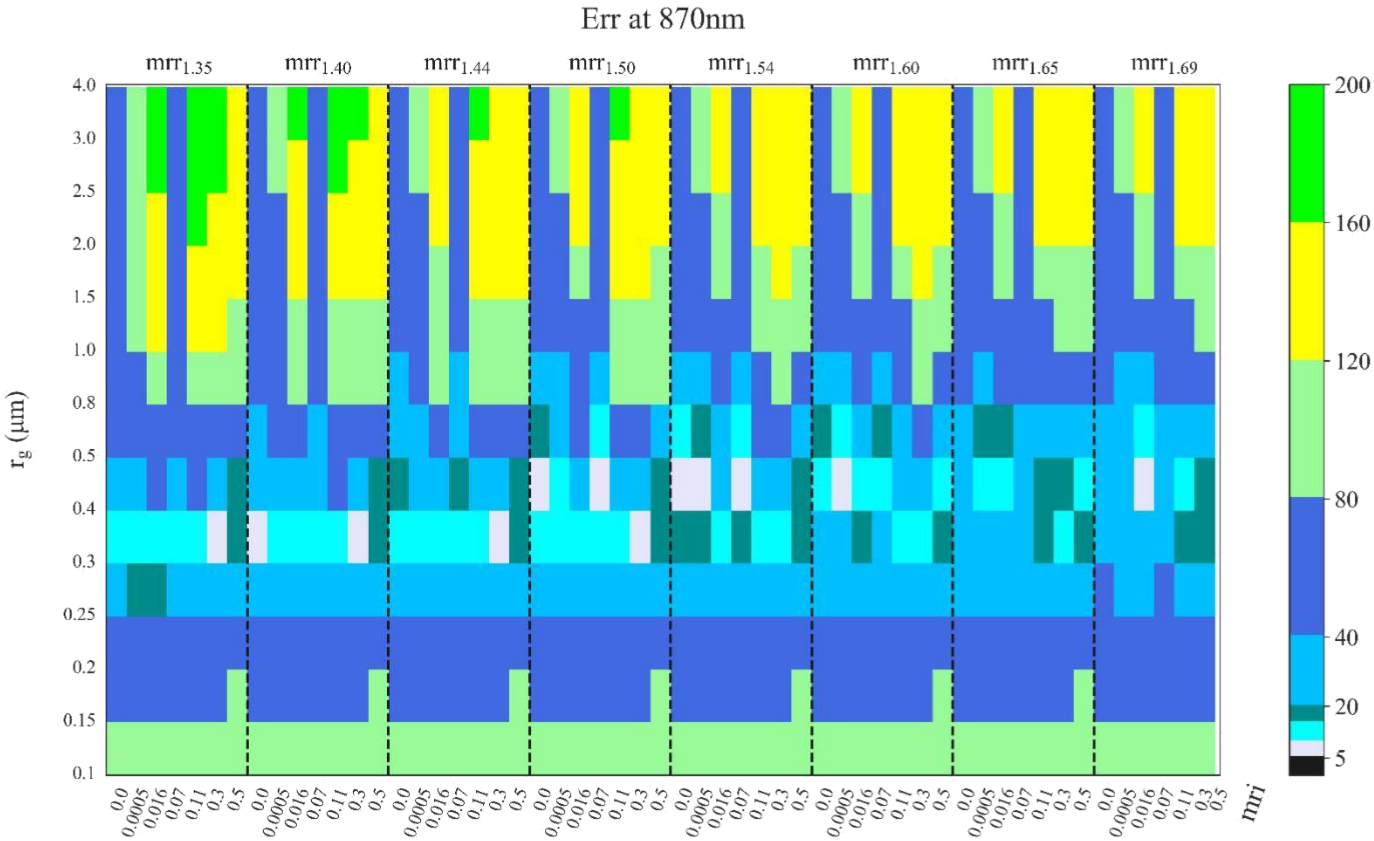

Figure S12. The residual error (Err) of fitting the phase functions at 870 nm of the near-spherical particles presented in the manuscript, with the phase functions calculated with the AERONET non-spherical model, for radius and complex refractive index shown in y- and x-axis, respectively

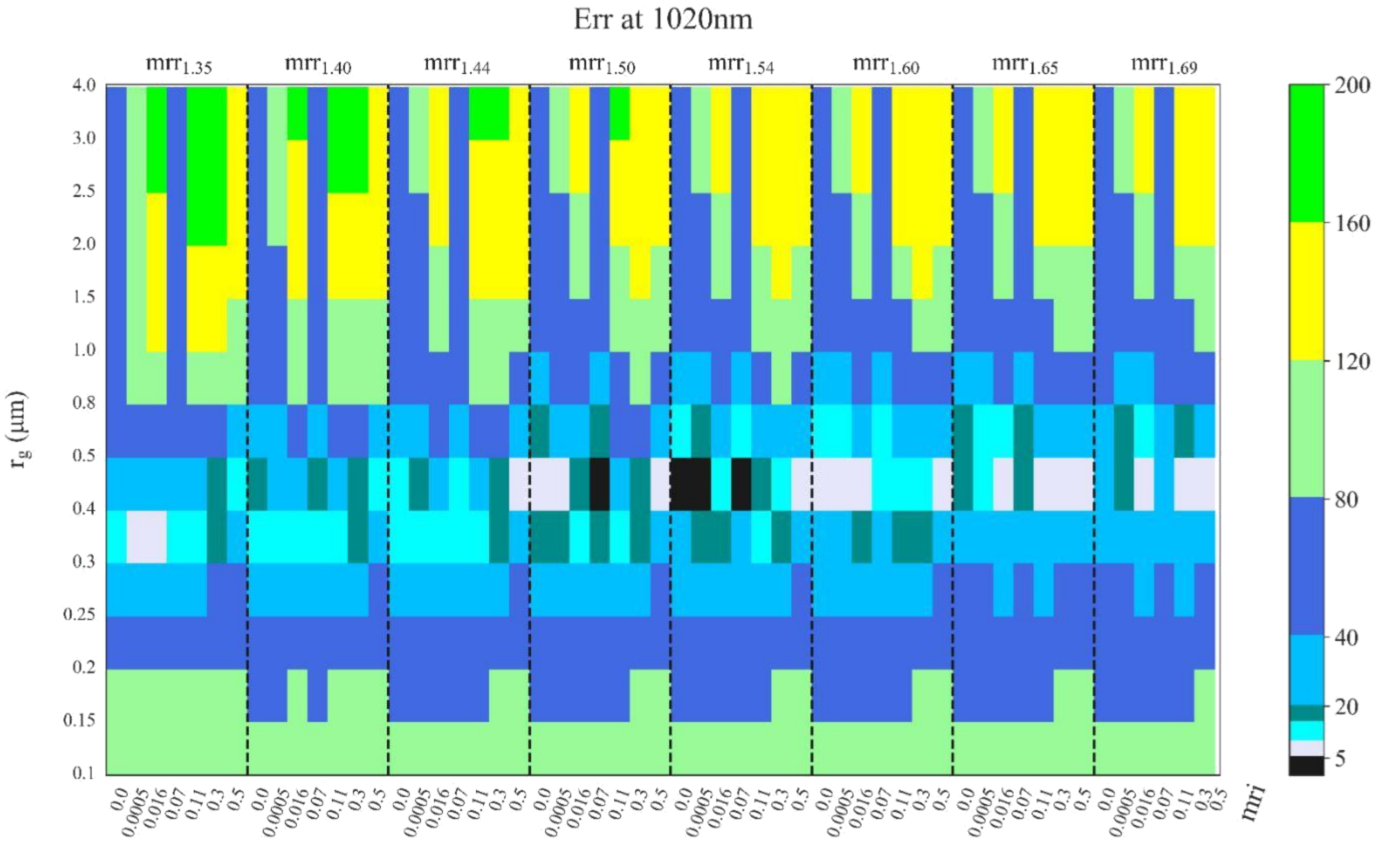

Figure S13. The residual error (Err) of fitting the phase functions at 1020 nm of the near-spherical particles presented in the manuscript, with the phase functions calculated with the AERONET non-spherical model, for radius and complex refractive index shown in y- and x-axis, respectively

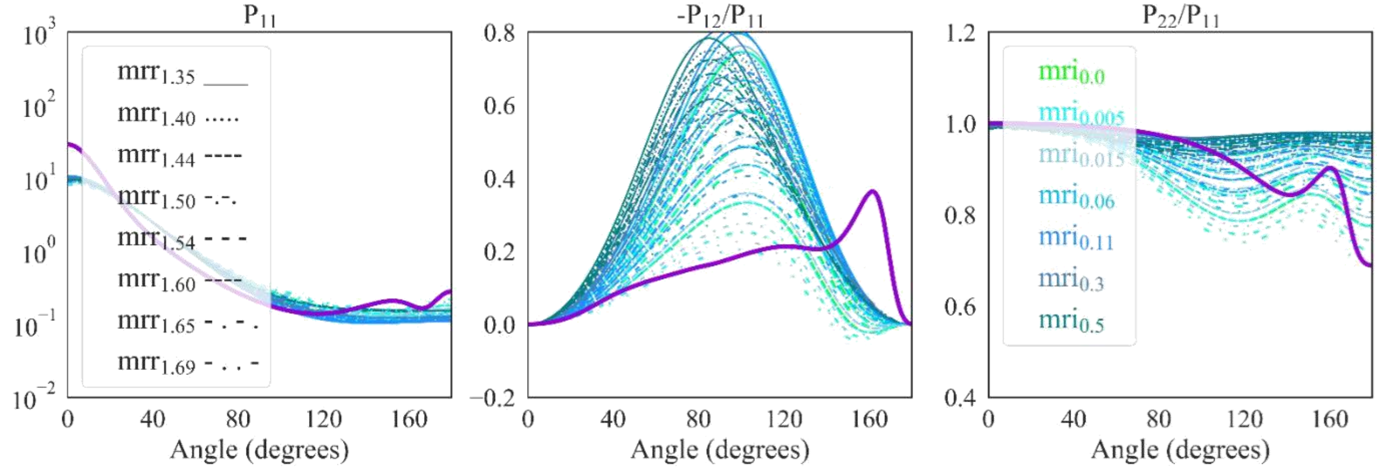

Figure S14. The elements of the scattering matrix at λ = 440nm. Left: P_{11} (phase function), middle: $-P_{12}/P_{11}$ (degree of linear polarization), right: P_{22}/P_{11}. Purple lines in the plots: calculations considering the near-spherical particle properties derived for the stratospheric smoke particles from the Canadian fires, with mean axial ratio ε_s = 1.3, mono-modal, log-normal size distribution with mean geometric radius r_g = 0.25 μm, geometric standard deviation σ_g = 0.4, and complex refractive index m = 1.55 – i0.03. Blue lines in the plots: calculations using the AERONET non-spherical model, mono-modal, log-normal size distributions with r_g = 0.1 μm and refractive indices of mrr = 1.35, 1.40, 1.44, 1.50, 1.54, 1.60, 1.65, 1.69 for the real part (different line styles in the plot) and mri = 0.0, 0.005, 0.015, 0.06, 0.11, 0.3, 0.5 for the imaginary part (different line colors in the plot).

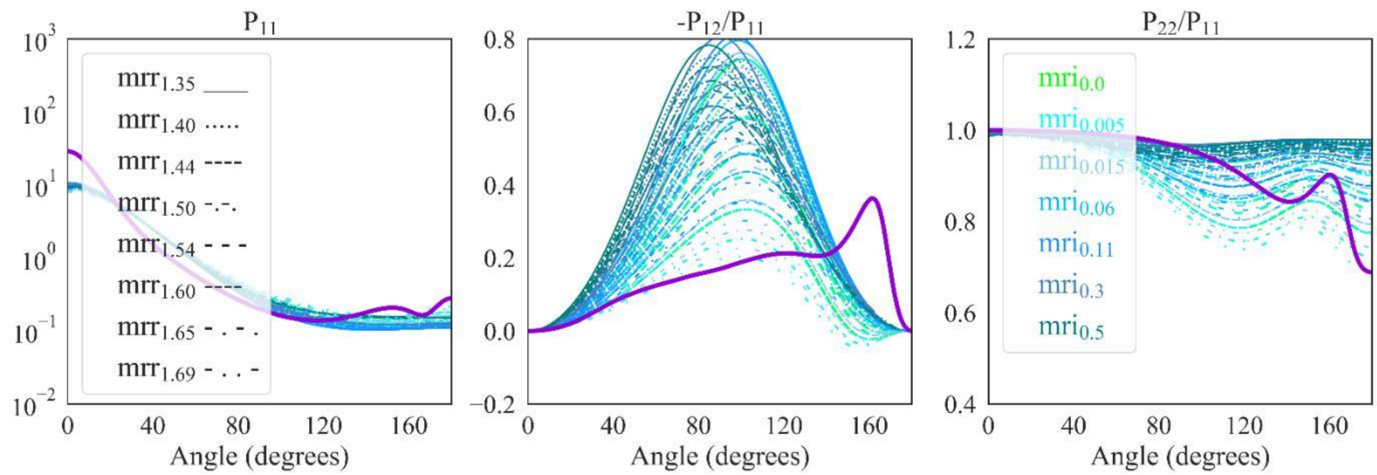

Figure S15. Same as Fig. S14, with the calculations using the AERONET non-spherical model, performed for mono-modal log-normal size distributions with mean geometric radius r_g = 0.15 μm.

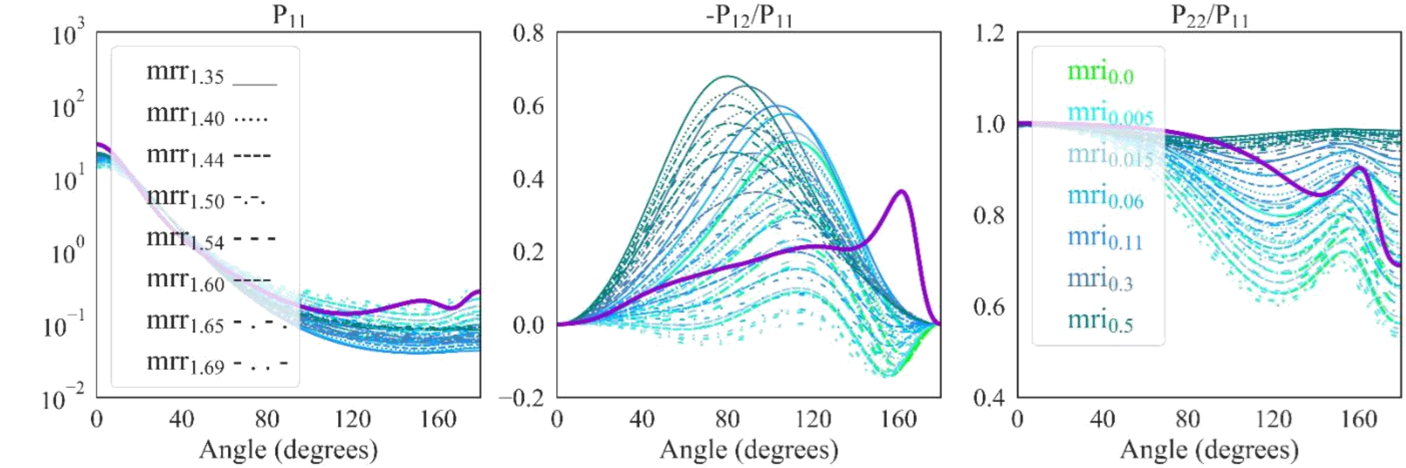

Figure S16. Same as Fig. S14, with the calculations using the AERONET non-spherical model, performed for mono-modal log-normal size distributions with mean geometric radius r_g = 0.2 μm

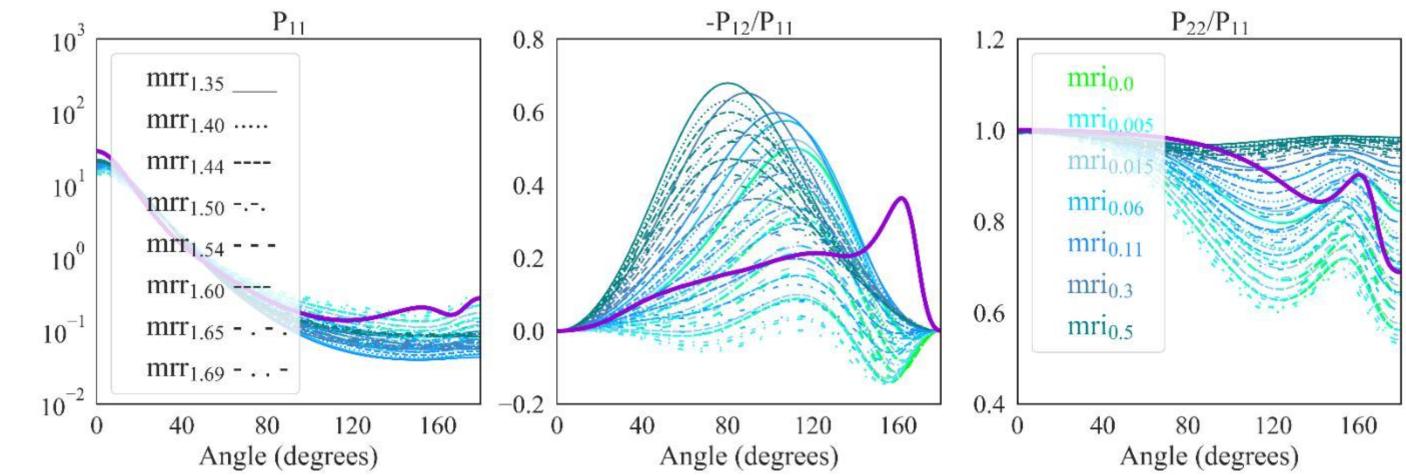

Figure S17. Same as Fig. S14, with the calculations using the AERONET non-spherical model, performed for mono-modal log-normal size distributions with mean geometric radius r_g = 0.25 μm

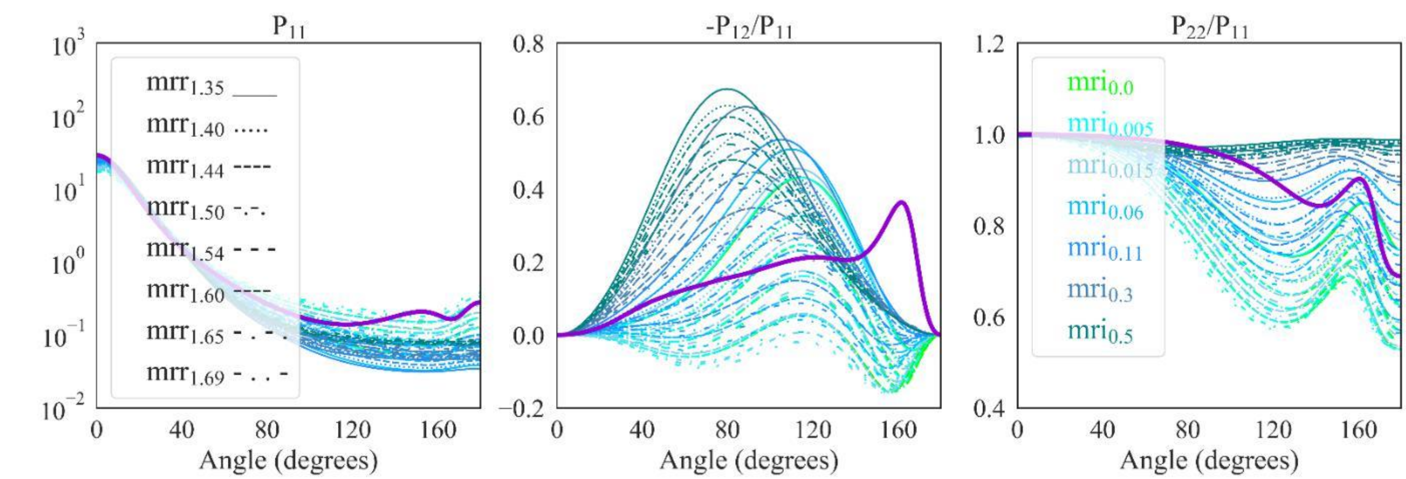

Figure S18. Same as Fig. S14, with the calculations using the AERONET non-spherical model, performed for mono-modal log-normal size distributions with mean geometric radius r_g = 0.3 μm.

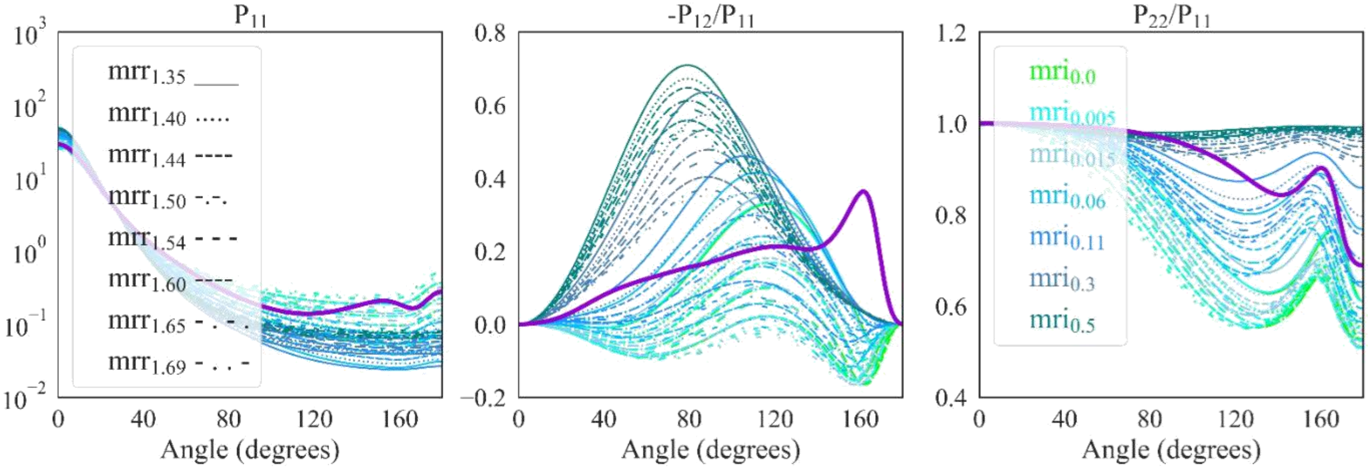

Figure S19. Same as Fig. S14, with the calculations using the AERONET non-spherical model, performed for mono-modal log-normal size distributions with mean geometric radius r_g = 0.4 μm.

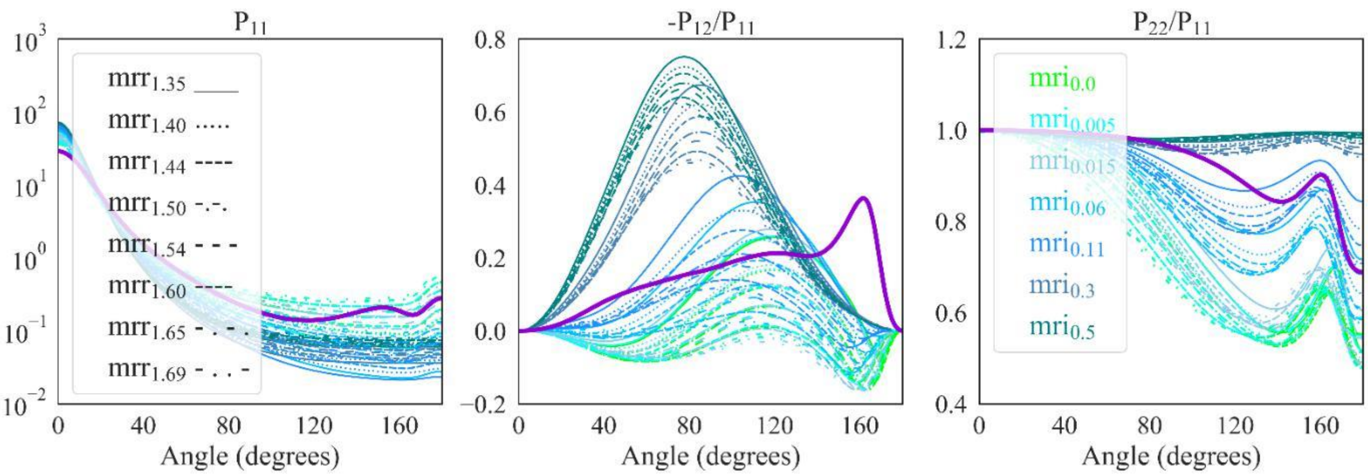

Figure S20. Same as Fig. S14, with the calculations using the AERONET non-spherical model, performed for mono-modal log-normal size distributions with mean geometric radius r_g = 0.5 μm.

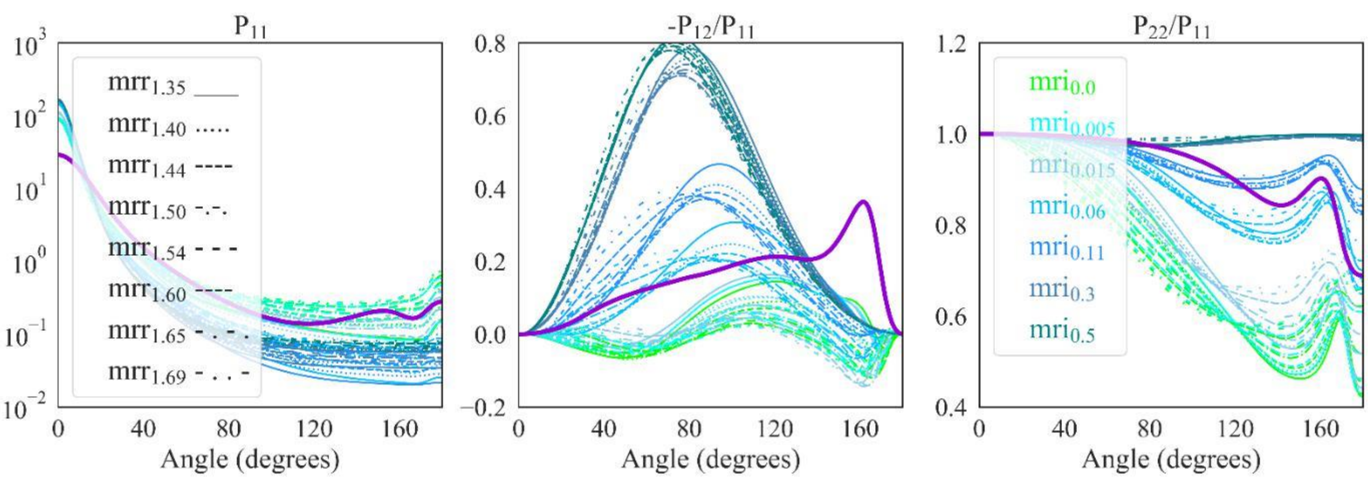

Figure S21. Same as Fig. S14, with the calculations using the AERONET non-spherical model, performed for mono-modal log-normal size distributions with mean geometric radius r_g = 0.8 μm.

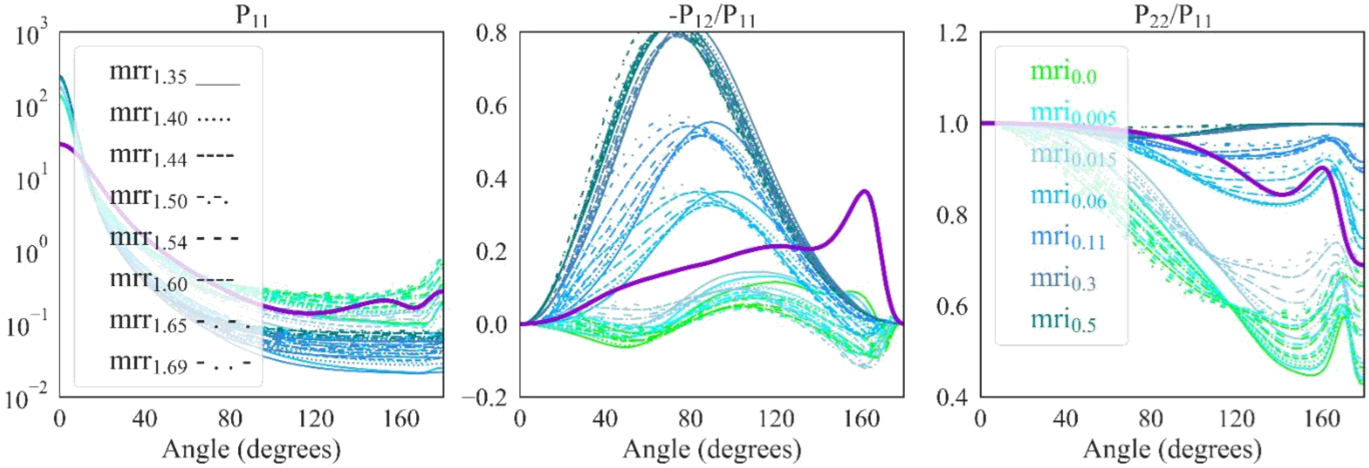

Figure S22. Same as Fig. S14, with the calculations using the AERONET non-spherical model, performed for mono-modal log-normal size distributions with mean geometric radius r_g = 1.0 μm.

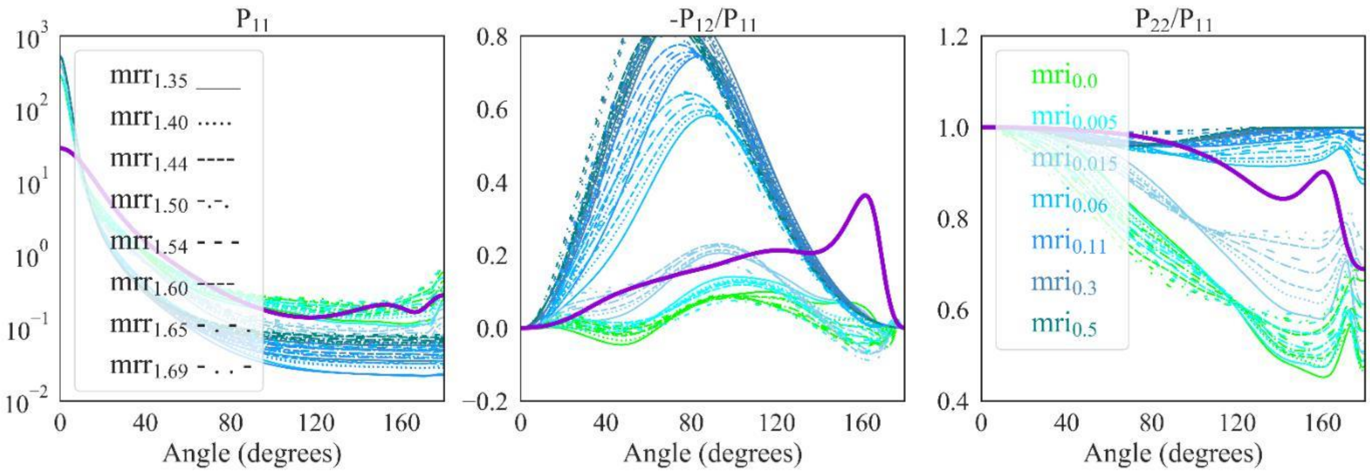

Figure S23. Same as Fig. S14, with the calculations using the AERONET non-spherical model, performed for mono-modal log-normal size distributions with mean geometric radius r_g = 1.5 μm.

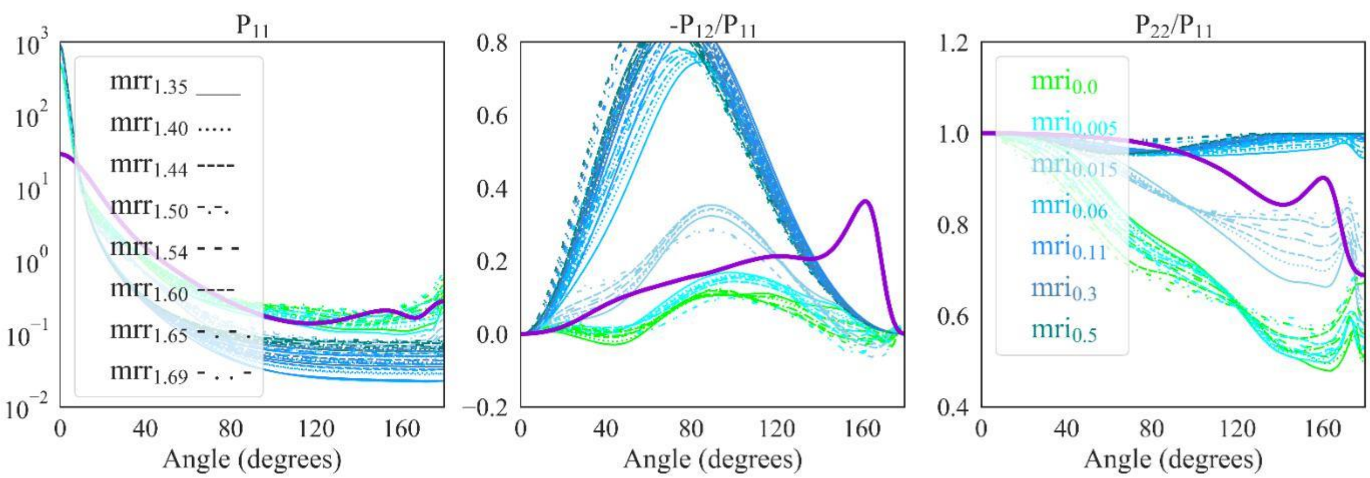

Figure S24. Same as Fig. S14, with the calculations using the AERONET non-spherical model, performed for mono-modal log-normal size distributions with mean geometric radius r_g = 2.0 μm.

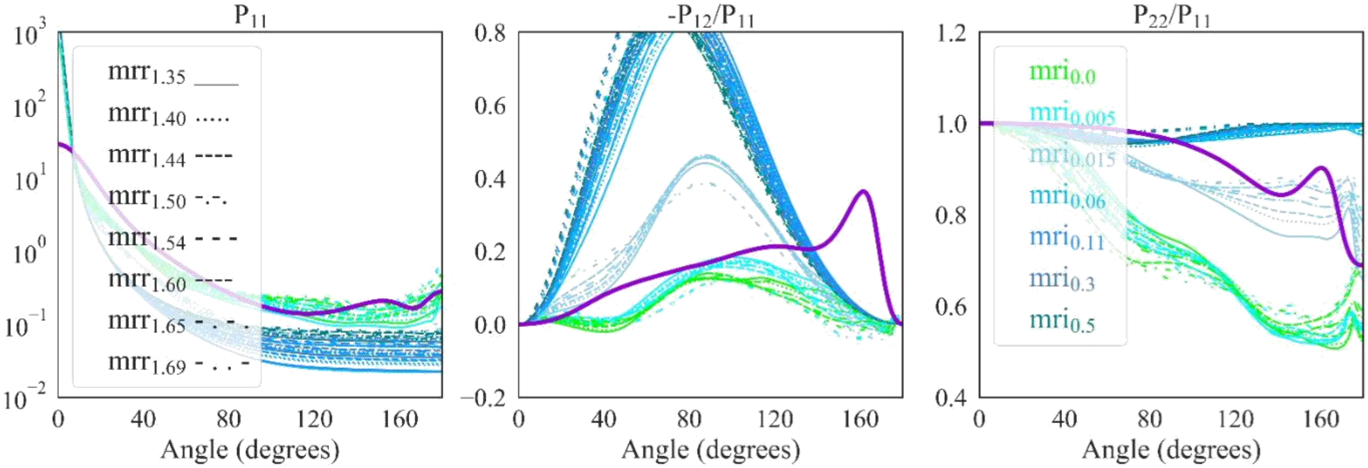

Figure S25. Same as Fig. S14, with the calculations using the AERONET non-spherical model, performed for mono-modal log-normal size distributions with mean geometric radius r_g = 2.5 μm.

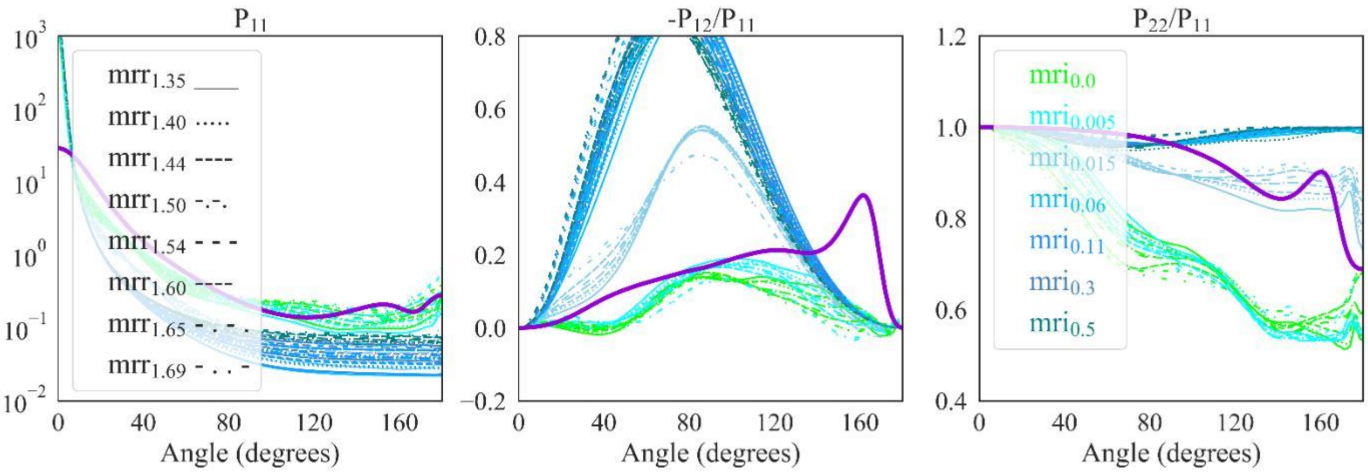

Figure S26. Same as Fig. S14, with the calculations using the AERONET non-spherical model, performed for mono-modal log-normal size distributions with mean geometric radius r_g = 3.0 μm.

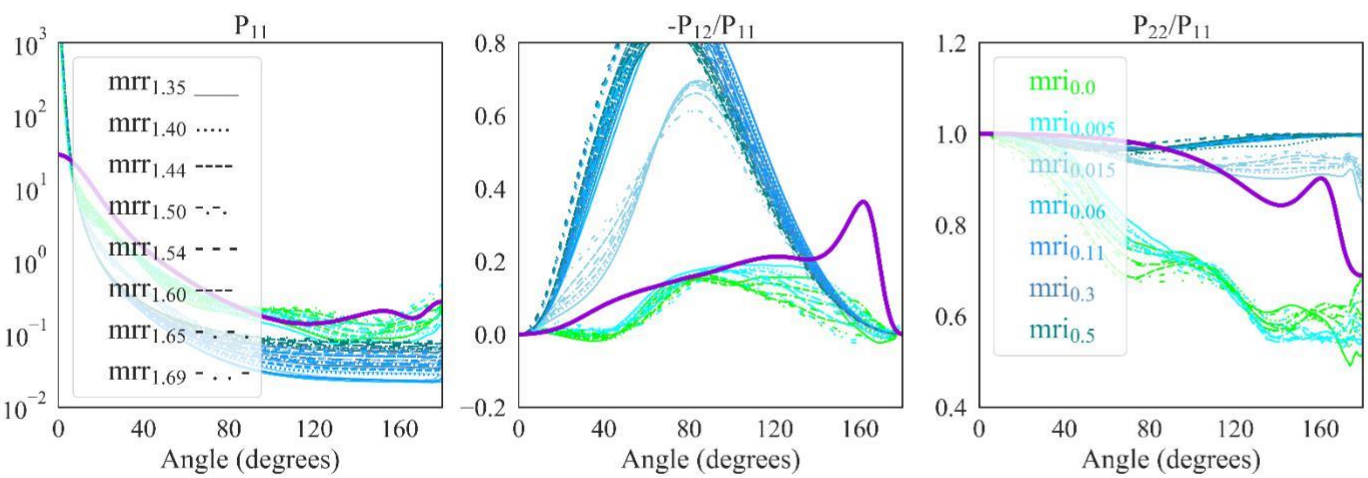

Figure S27. Same as Fig. S14, with the calculations using the AERONET non-spherical model, performed for mono-modal log-normal size distributions with mean geometric radius r_g = 4.0 μm.

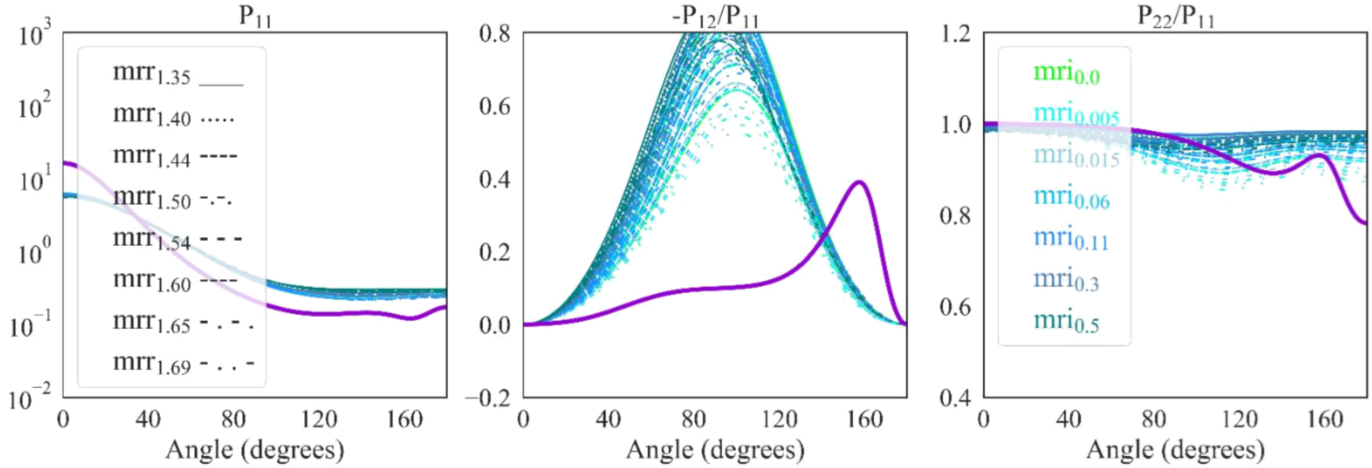

Figure S28. The elements of the scattering matrix at λ = 670 nm. Left: P_{11} (phase function), middle: $-P_{12}/P_{11}$ (degree of linear polarization), right: P_{22}/P_{11}. Purple lines in the plots: calculations considering the near-spherical particle properties derived for the stratospheric smoke particles from the Canadian fires, with mean axial ratio ε_s = 1.3, mono-modal, log-normal size distribution with mean geometric radius r_g = 0.25 μm, mean geometric standard deviation σ_g = 0.4, and complex refractive index m = 1.55 – i0.03. Blue lines in the plots: calculations using the AERONET non-spherical model, mono-modal, log-normal size distributions with r_g = 0.1 μm and refractive indices of mrr = 1.35, 1.40, 1.44, 1.50, 1.54, 1.60, 1.65, 1.69 for the real part (different line styles in the plot) and mri = 0.0, 0.005, 0.015, 0.06, 0.11, 0.3, 0.5 for the imaginary part (different line colors in the plot).

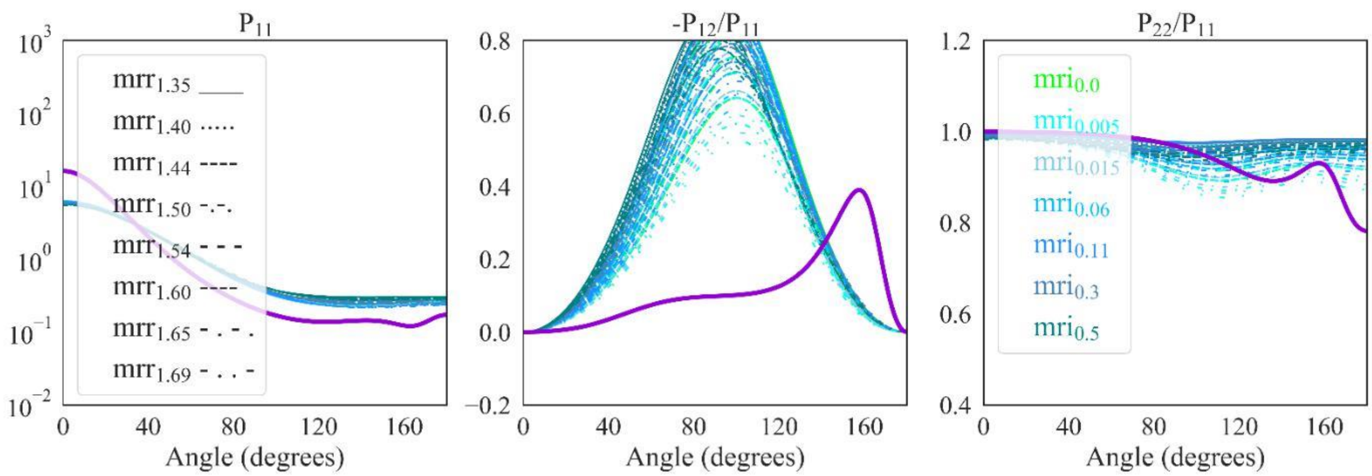

Figure S29. Same as Fig. S28, with the calculations using the AERONET non-spherical model, performed for mono-modal log-normal size distributions with mean geometric radius r_g = 0.15 μm

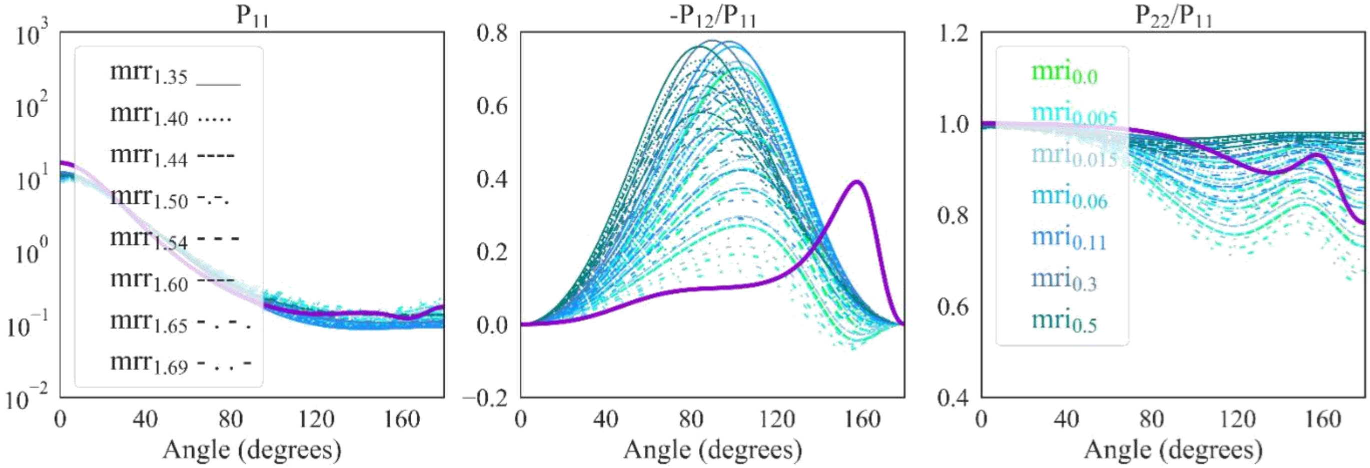

Figure S30. Same as Fig. S28, with the calculations using the AERONET non-spherical model, performed for mono-modal log-normal size distributions with mean geometric radius r_g = 0.2 μm.

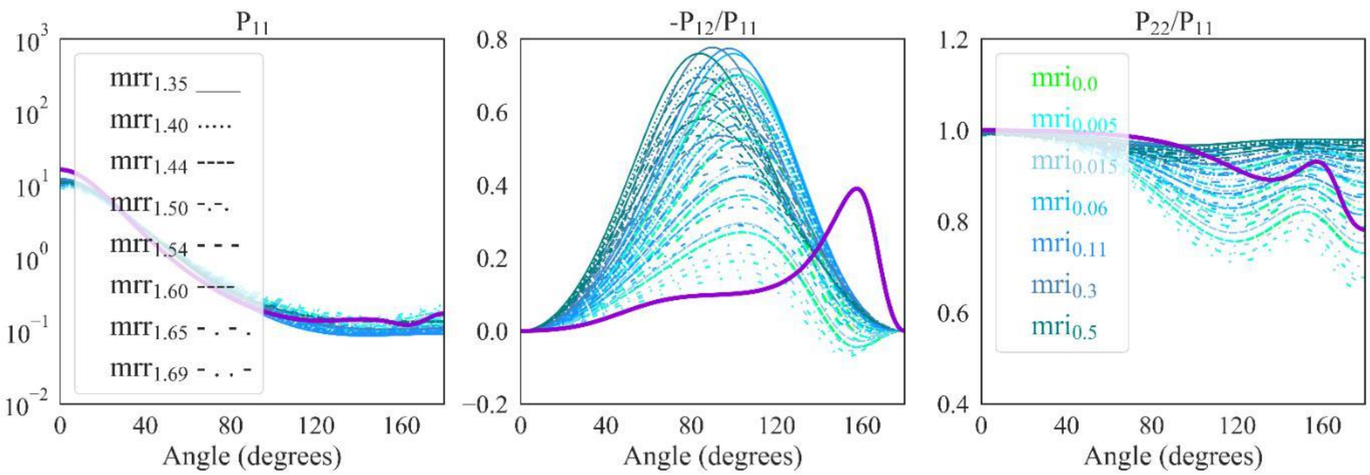

Figure S31. Same as Fig. S28, with the calculations using the AERONET non-spherical model, performed for mono-modal log-normal size distributions with mean geometric radius r_g = 0.25 μm.

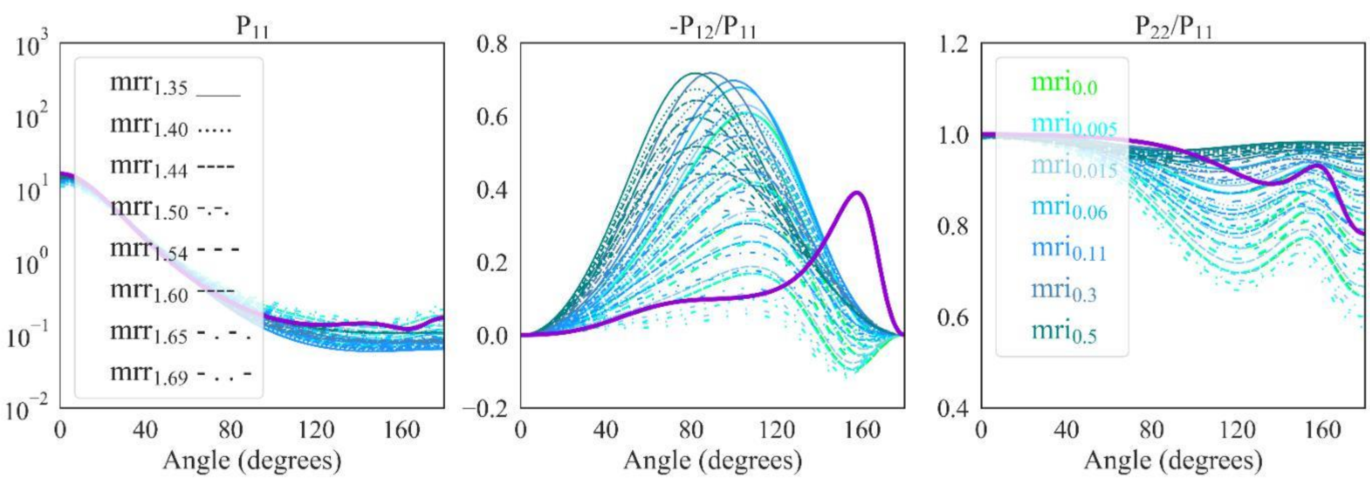

Figure S32. Same as Fig. S28, with the calculations using the AERONET non-spherical model, performed for mono-modal log-normal size distributions with mean geometric radius r_g = 0.3 μm.

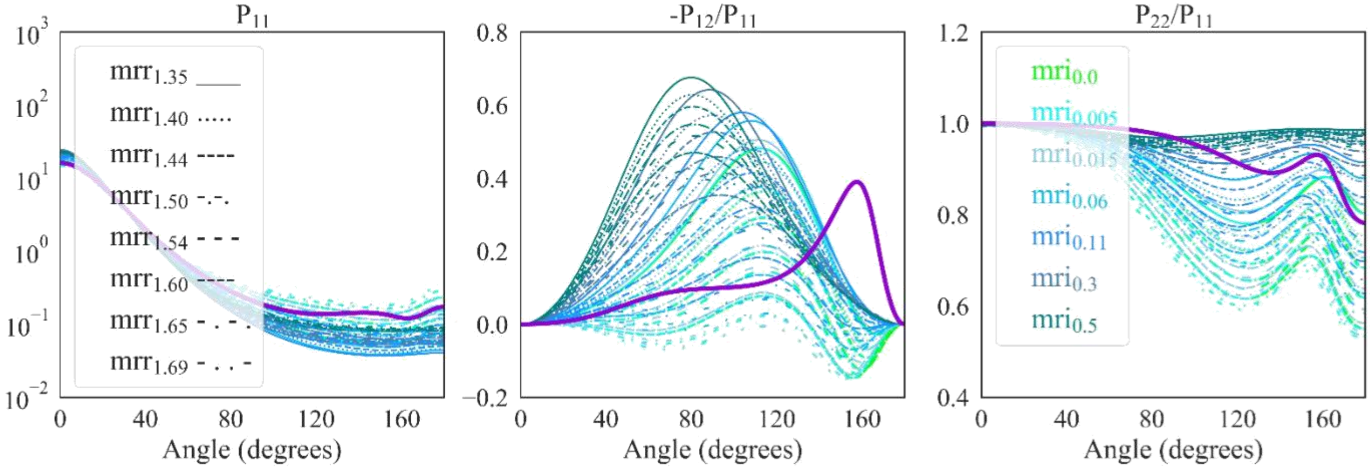

Figure S33. Same as Fig. S28, with the calculations using the AERONET non-spherical model, performed for mono-modal log-normal size distributions with mean geometric radius r_g = 0.4 μm.

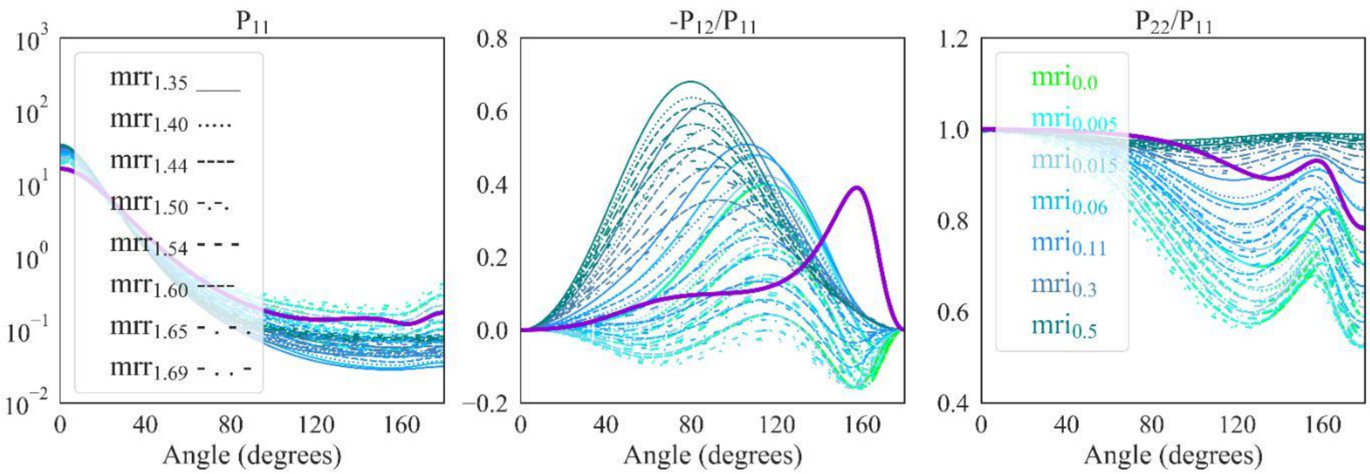

Figure S34. Same as Fig. S28, with the calculations using the AERONET non-spherical model, performed for mono-modal log-normal size distributions with mean geometric radius r_g = 0.5 μm.

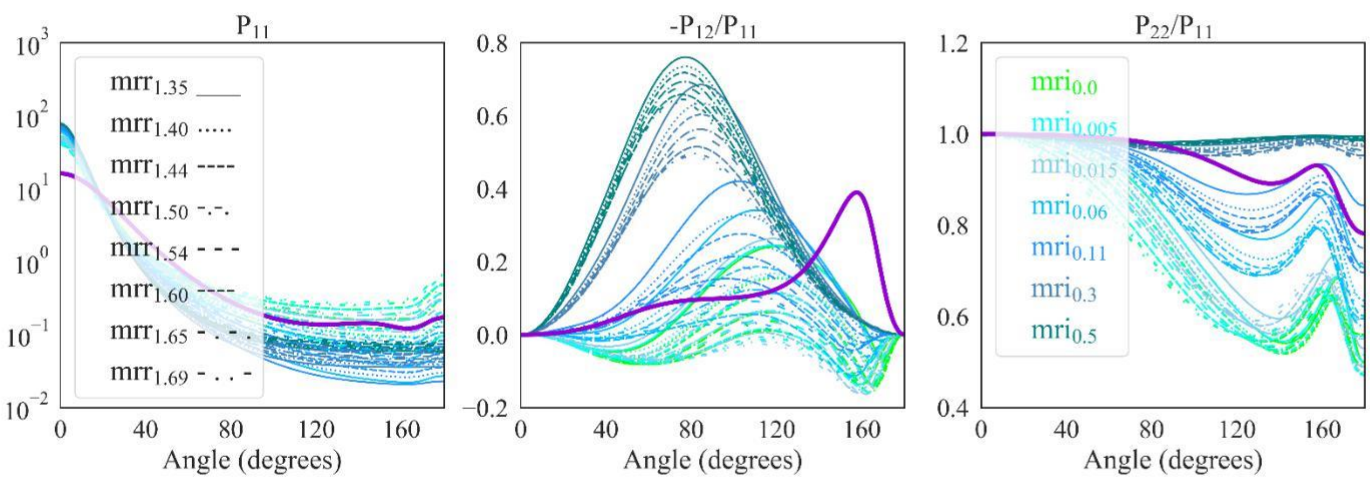

Figure S35. Same as Fig. S28, with the calculations using the AERONET non-spherical model, performed for mono-modal log-normal size distributions with mean geometric radius r_g = 0.8 μm.

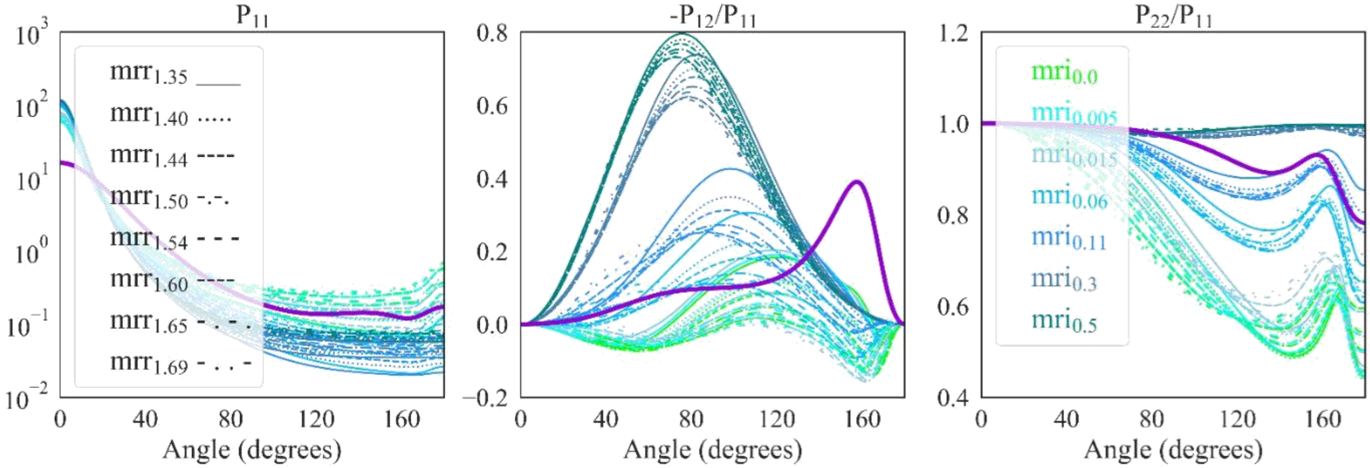

Figure S36. Same as Fig. S28, with the calculations using the AERONET non-spherical model, performed for mono-modal log-normal size distributions with mean geometric radius r_g = 1.0 μm.

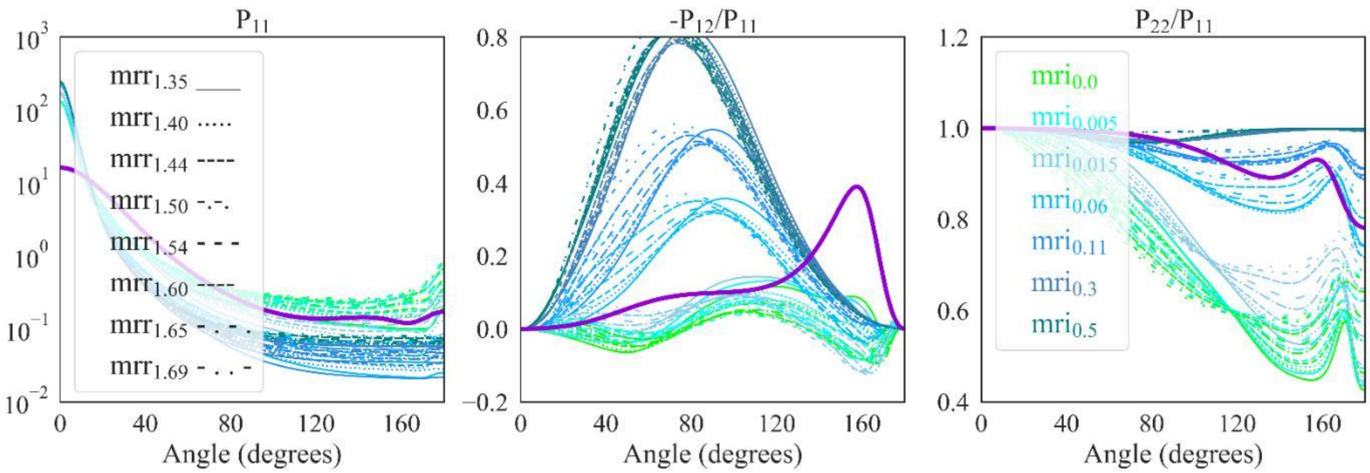

Figure S37. Same as Fig. S28, with the calculations using the AERONET non-spherical model, performed for mono-modal log-normal size distributions with mean geometric radius r_g = 1.5 μm.

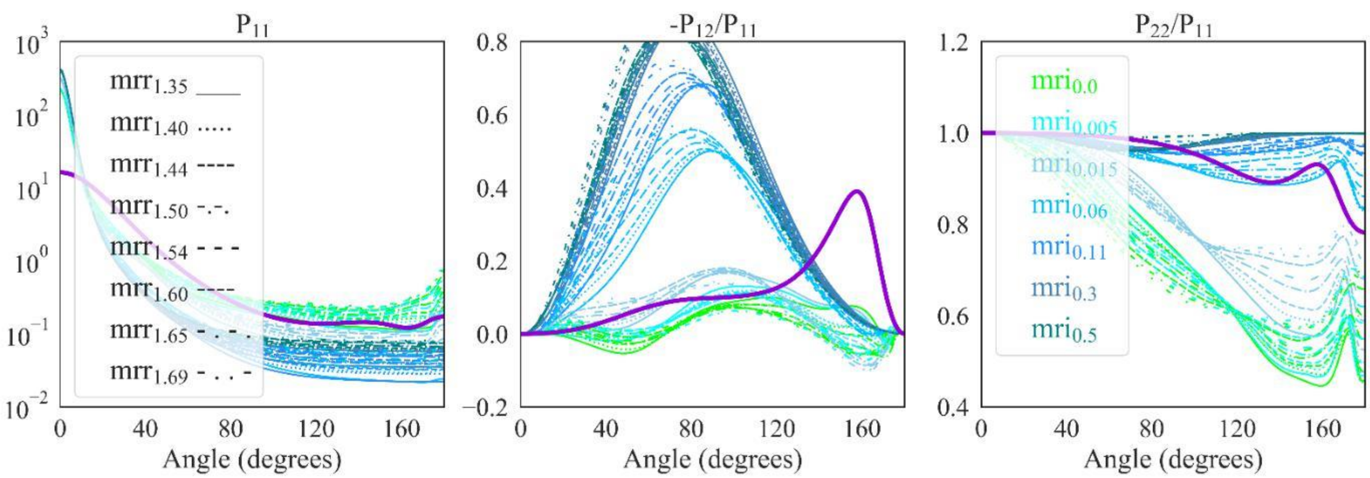

Figure S38. Same as Fig. S28, with the calculations using the AERONET non-spherical model, performed for mono-modal log-normal size distributions with mean geometric radius r_g = 2.0 μm.

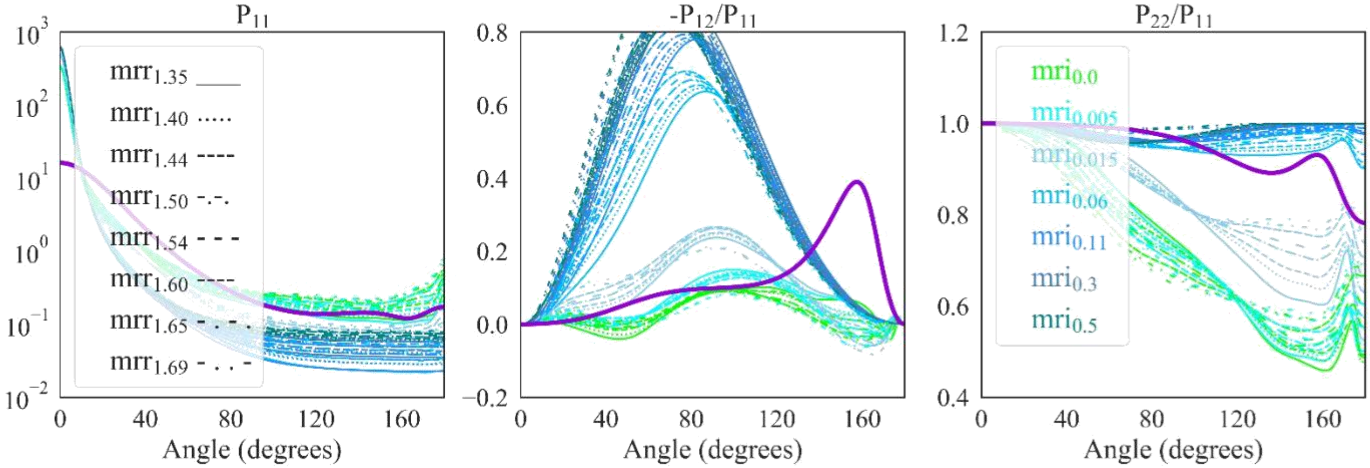

Figure S39. Same as Fig. S28, with the calculations using the AERONET non-spherical model, performed for mono-modal log-normal size distributions with mean geometric radius r_g = 2.5 μm.

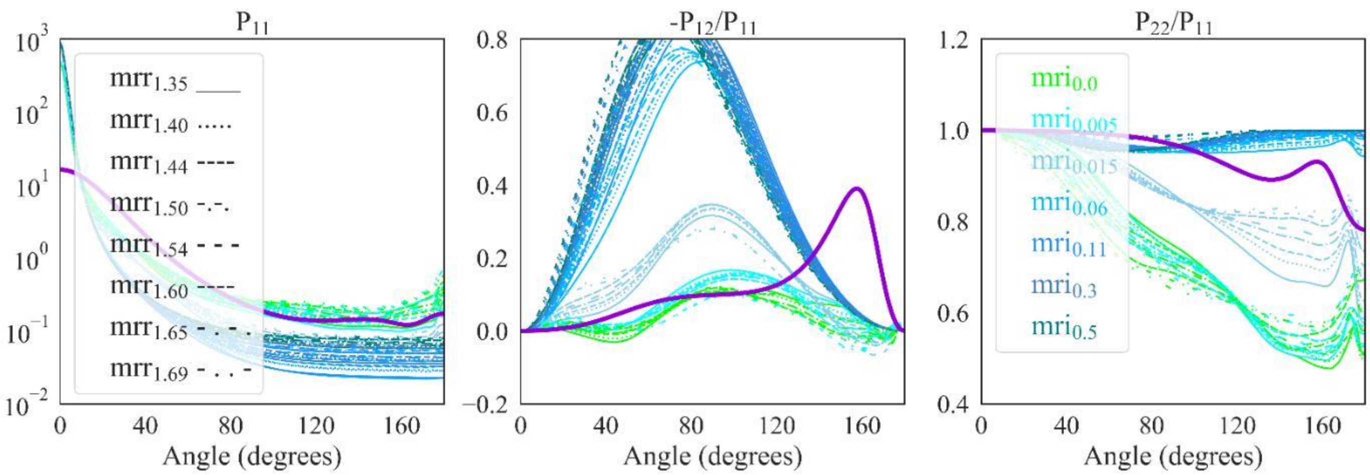

Figure S40. Same as Fig. S28, with the calculations using the AERONET non-spherical model, performed for mono-modal log-normal size distributions with mean geometric radius r_g = 3.0 μm.

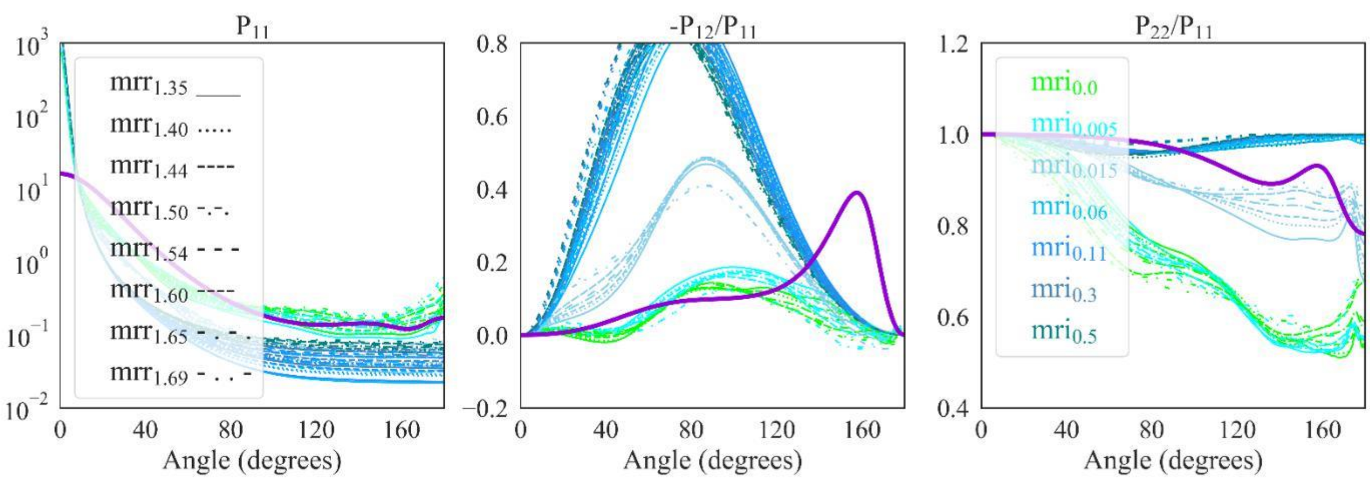

Figure S41. Same as Fig. S28, with the calculations using the AERONET non-spherical model, performed for mono-modal log-normal size distributions with mean geometric radius r_g = 4.0 μm.

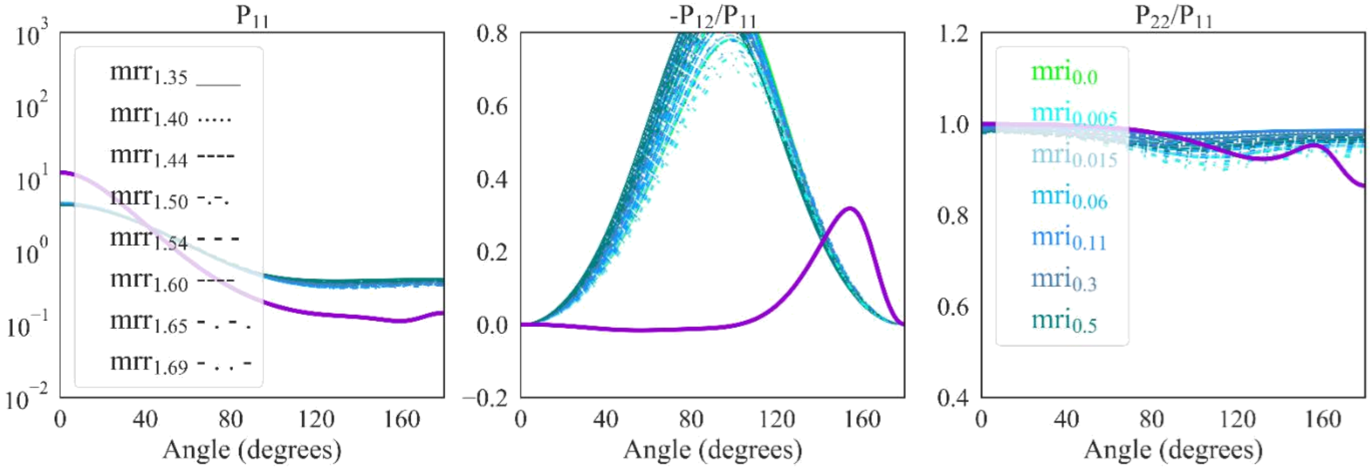

Figure S42. The elements of the scattering matrix at λ = 870 nm. Left: P11 (phase function), middle: -P12/P11 (degree of linear polarization), right: P22/P11. Purple lines in the plots: calculations considering the near-spherical particle properties derived for the stratospheric smoke particles from the Canadian fires, with mean axial ratio ε_s = 1.3, mono-modal, log-normal size distribution with mean geometric radius r_g = 0.25 μm, mean geometric standard deviation σ_g = 0.4, and complex refractive index m = 1.55 – i0.03. Blue lines in the plots: calculations using the AERONET non-spherical model, mono-modal, log-normal size distributions with r_g = 0.1μm and refractive indices of mrr = 1.35, 1.40, 1.44, 1.50, 1.54, 1.60, 1.65, 1.69 for the real part (different line styles in the plot) and mri = 0.0, 0.005, 0.015, 0.06, 0.11, 0.3, 0.5 for the imaginary part (different line colors in the plot).

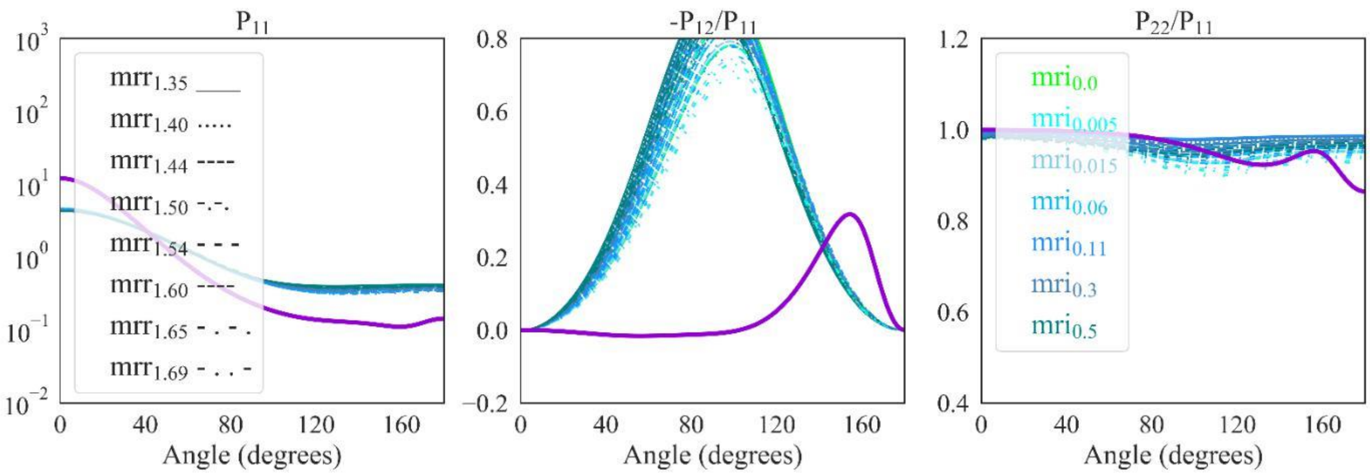

Figure S43. Same as Fig. S42, with the calculations using the AERONET non-spherical model, performed for mono-modal log-normal size distributions with mean geometric radius r_g = 0.15 μm.

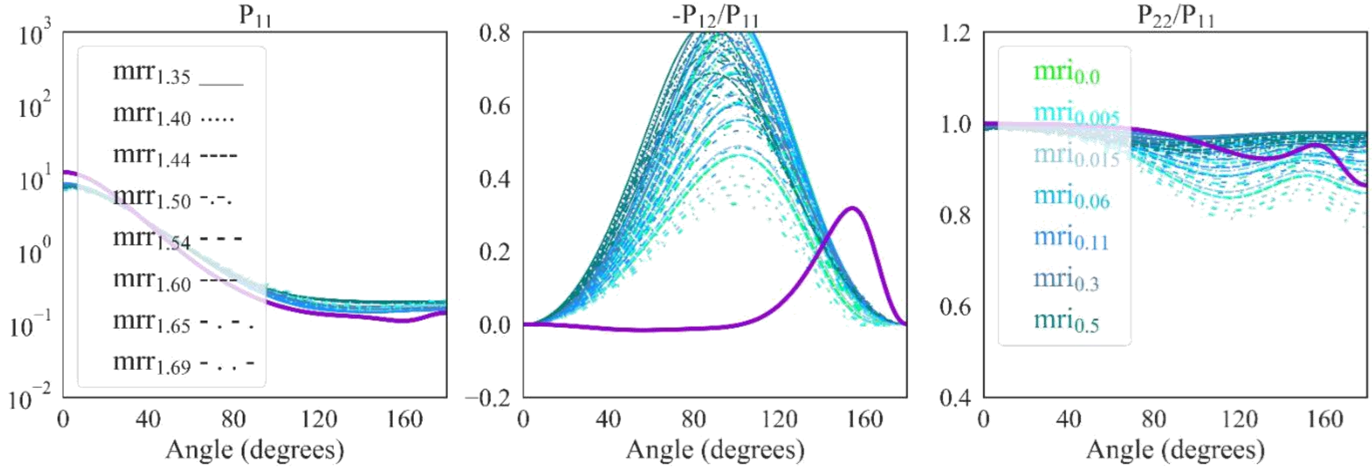

Figure S44. Same as Fig. S42, with the calculations using the AERONET non-spherical model, performed for mono-modal log-normal size distributions with mean geometric radius r_g = 0.2 μm.

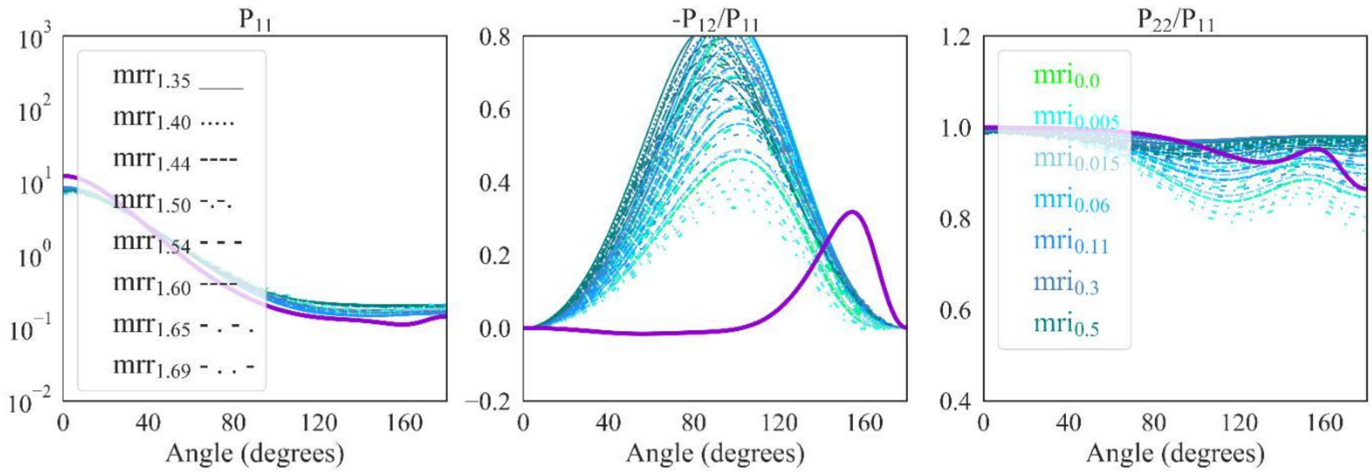

Figure S45. Same as Fig. S42, with the calculations using the AERONET non-spherical model, performed for mono-modal log-normal size distributions with mean geometric radius r_g = 0.25 μm.

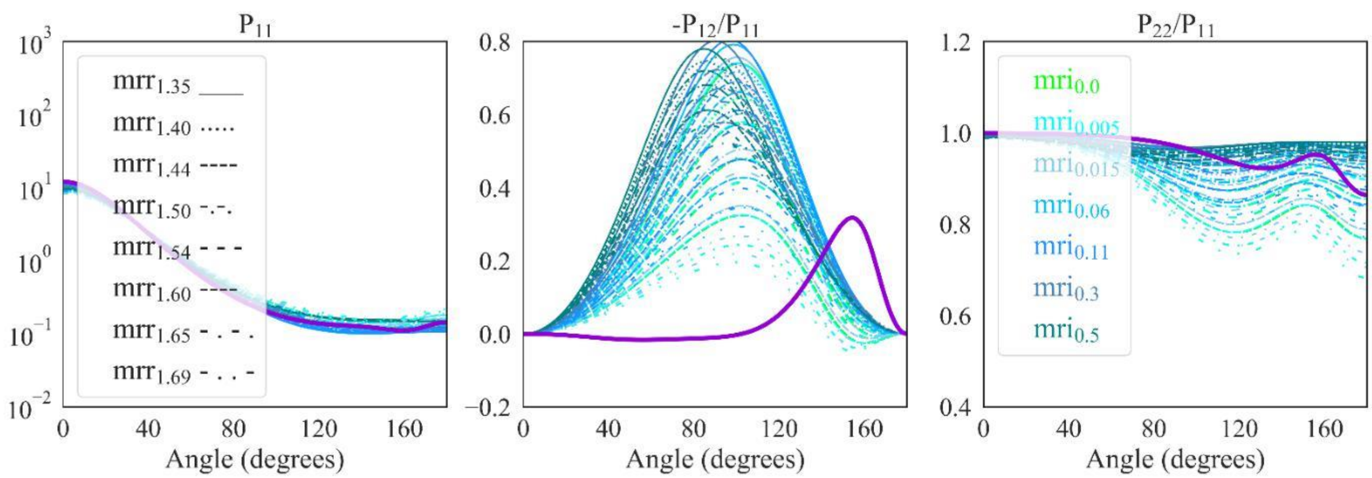

Figure S46. Same as Fig. S42, with the calculations using the AERONET non-spherical model, performed for mono-modal log-normal size distributions with mean geometric radius r_g = 0.3 μm.

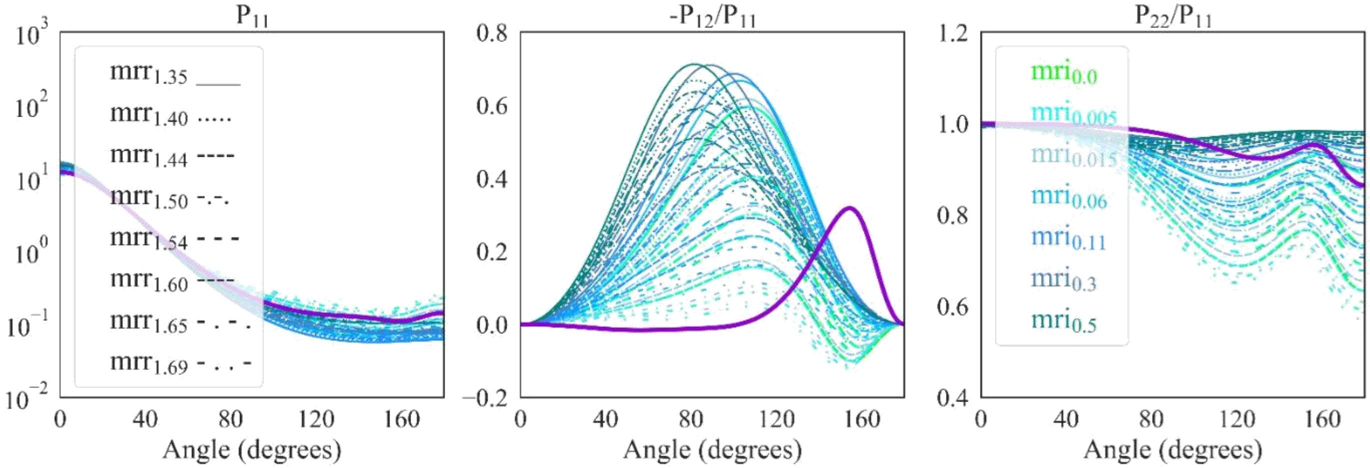

Figure S47. Same as Fig. S42, with the calculations using the AERONET non-spherical model, performed for mono-modal log-normal size distributions with mean geometric radius r_g = 0.4 μm.

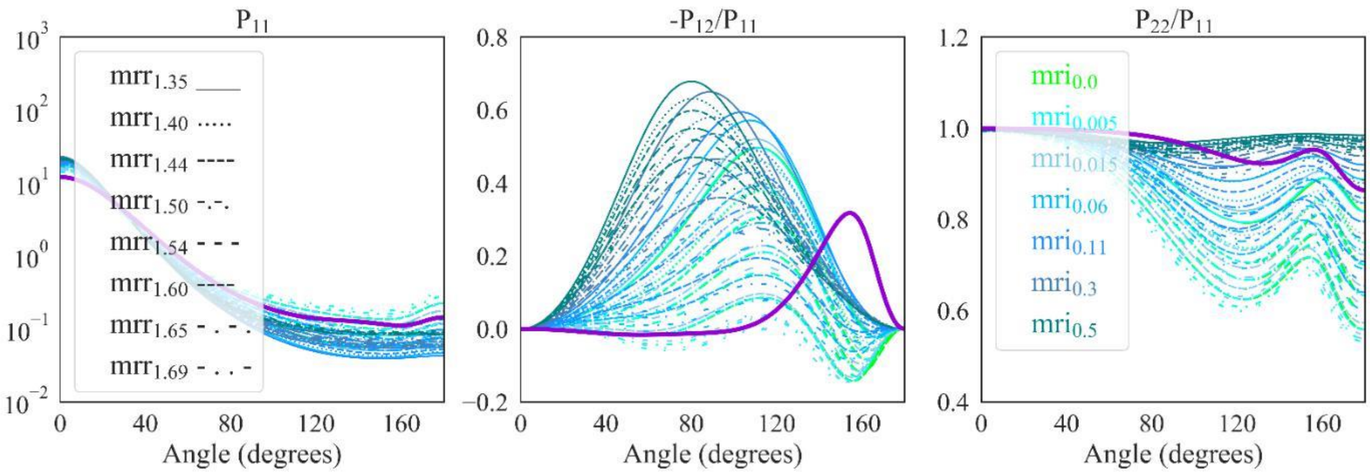

Figure S48. Same as Fig. S42, with the calculations using the AERONET non-spherical model, performed for mono-modal log-normal size distributions with mean geometric radius r_g = 0.5 μm.

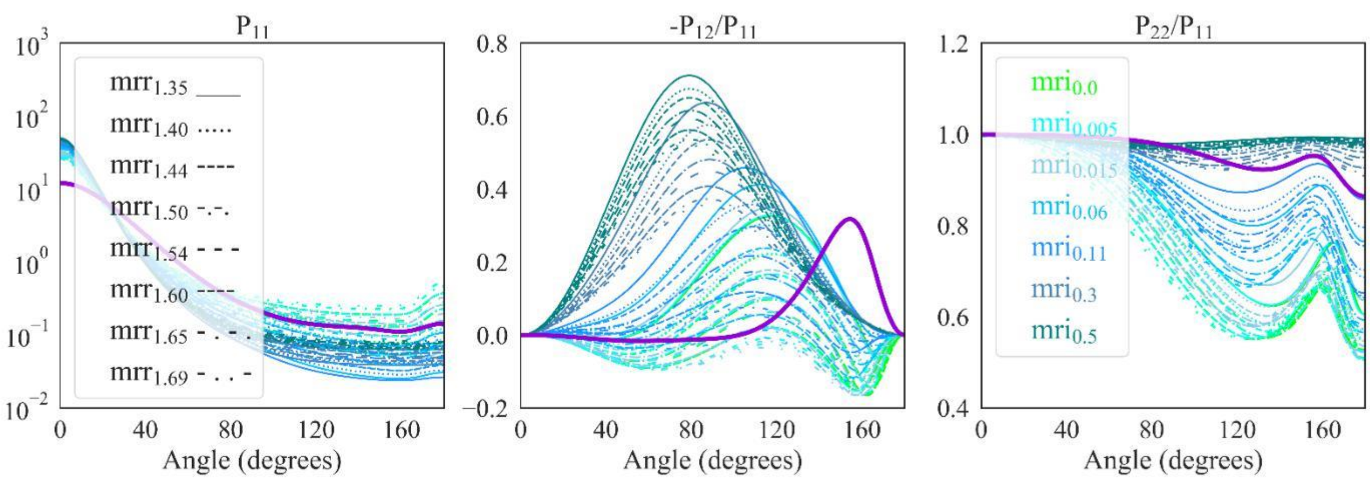

Figure S49. Same as Fig. S42, with the calculations using the AERONET non-spherical model, performed for mono-modal log-normal size distributions with mean geometric radius r_g = 0.8 μm.

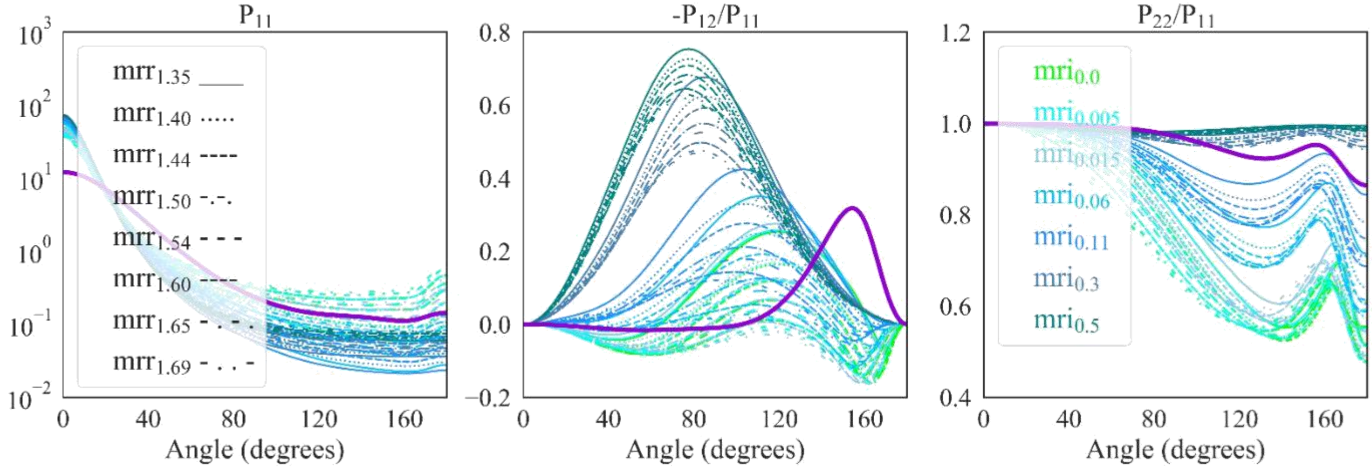

Figure S50. Same as Fig. S42, with the calculations using the AERONET non-spherical model, performed for mono-modal log-normal size distributions with mean geometric radius r_g = 1.0 μm.

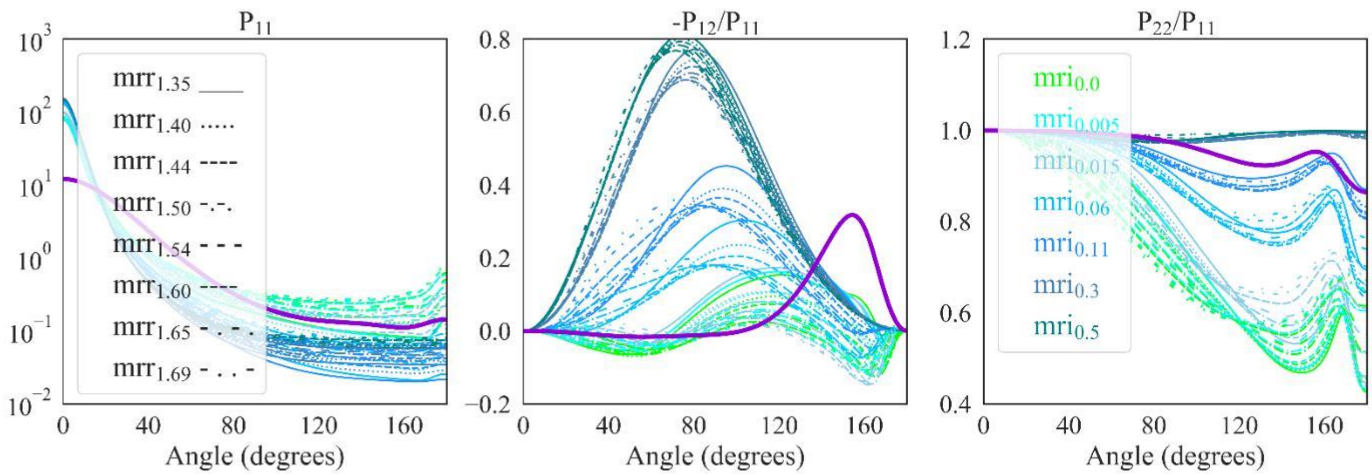

Figure S51. Same as Fig. S42, with the calculations using the AERONET non-spherical model, performed for mono-modal log-normal size distributions with mean geometric radius r_g = 1.5 μm.

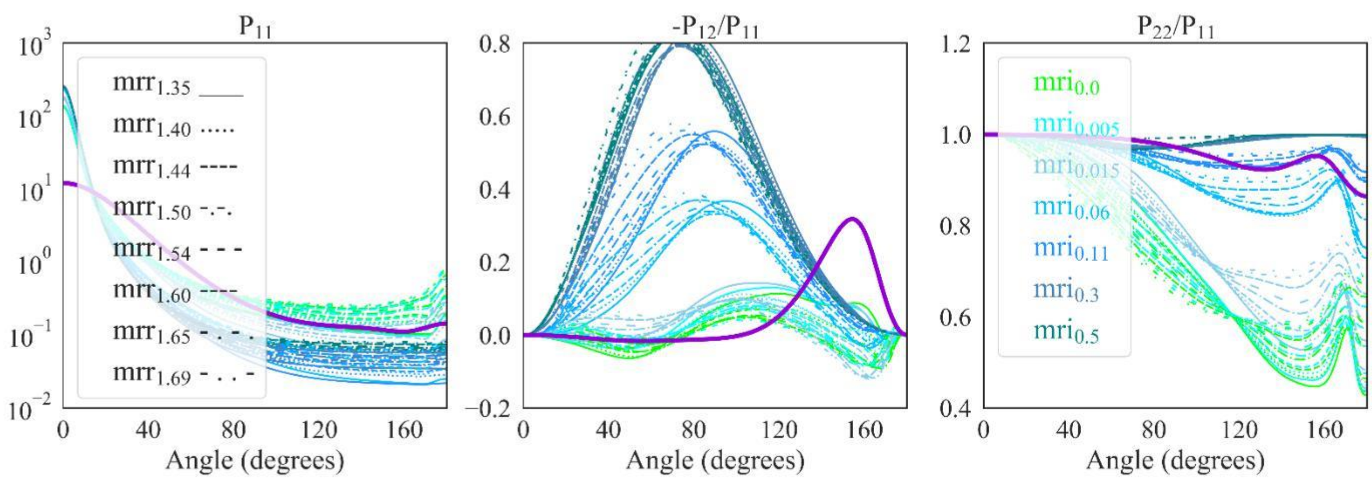

Figure S52. Same as Fig. S42, with the calculations using the AERONET non-spherical model, performed for mono-modal log-normal size distributions with mean geometric radius r_g = 2.0 μm.

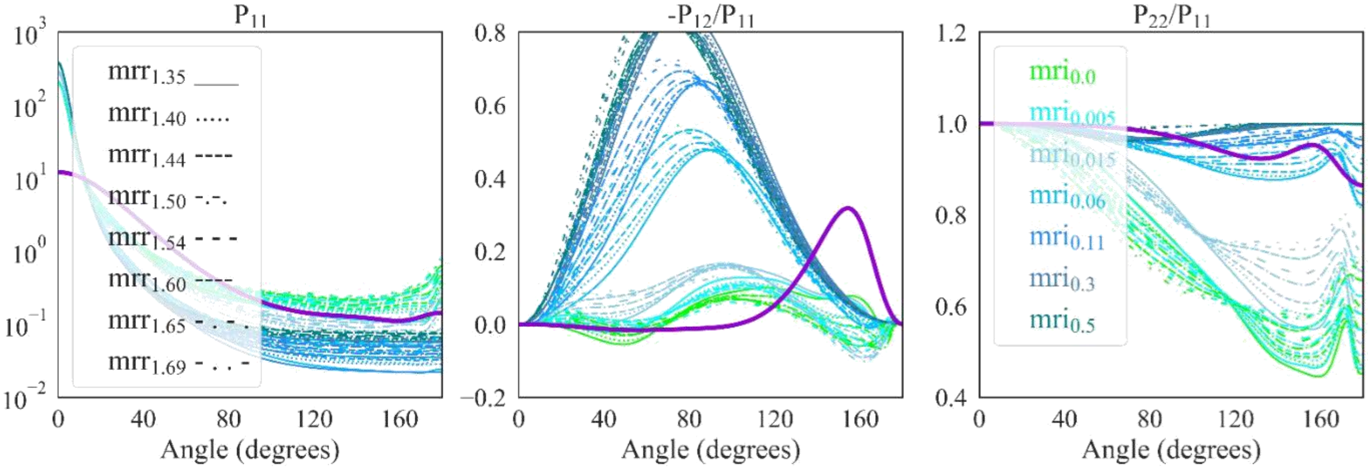

Figure S53. Same as Fig. S42, with the calculations using the AERONET non-spherical model, performed for mono-modal log-normal size distributions with mean geometric radius r_g = 2.5 μm.

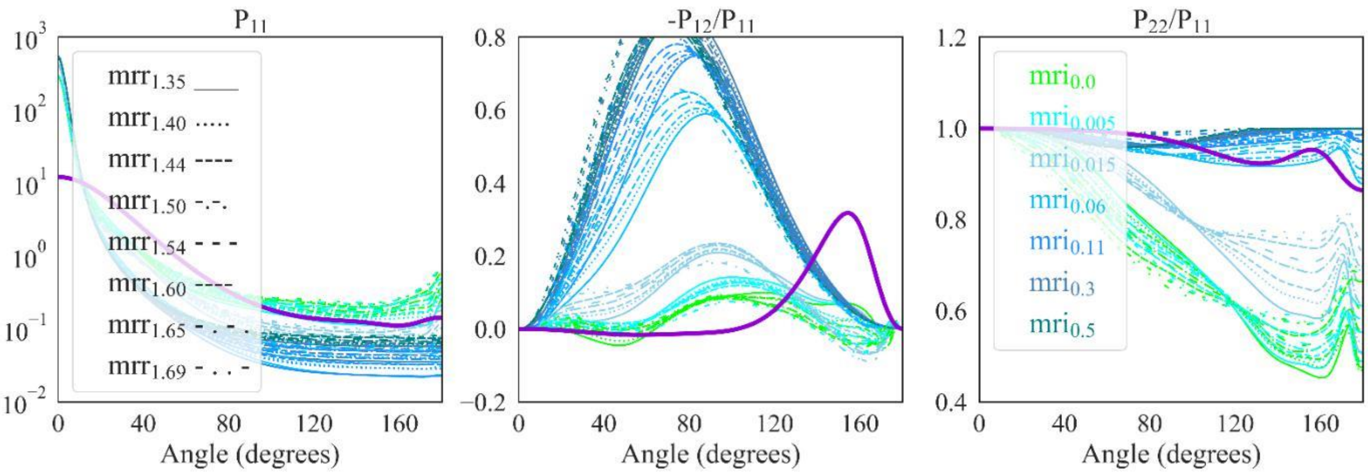

Figure S54. Same as Fig. S42, with the calculations using the AERONET non-spherical model, performed for mono-modal log-normal size distributions with mean geometric radius r_g = 3.0 μm.

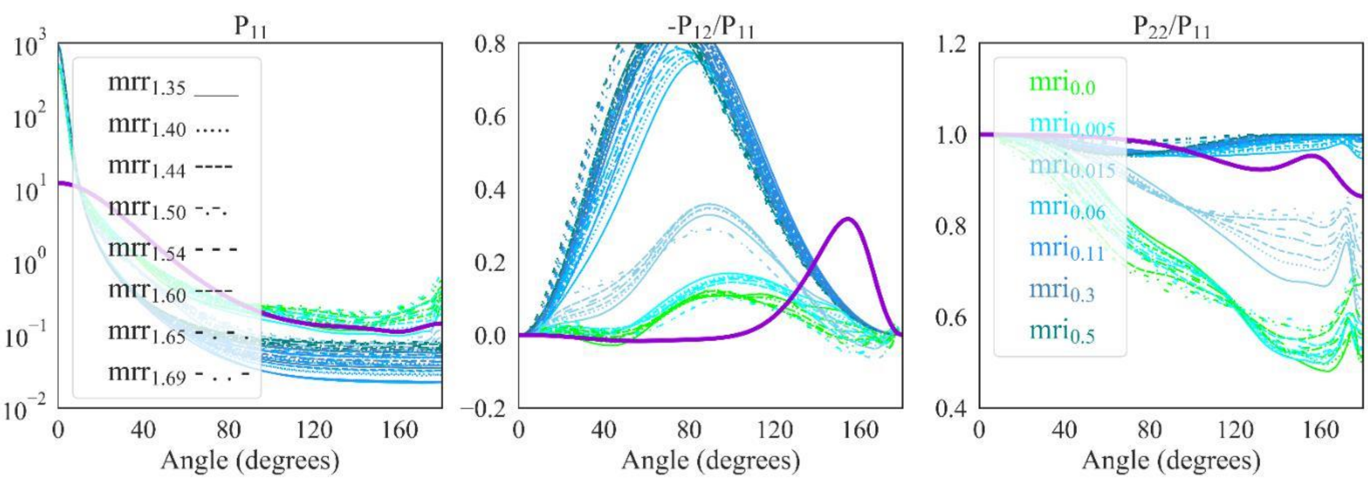

Figure S55. Same as Fig. S42, with the calculations using the AERONET non-spherical model, performed for mono-modal log-normal size distributions with mean geometric radius r_g = 4.0 µm.

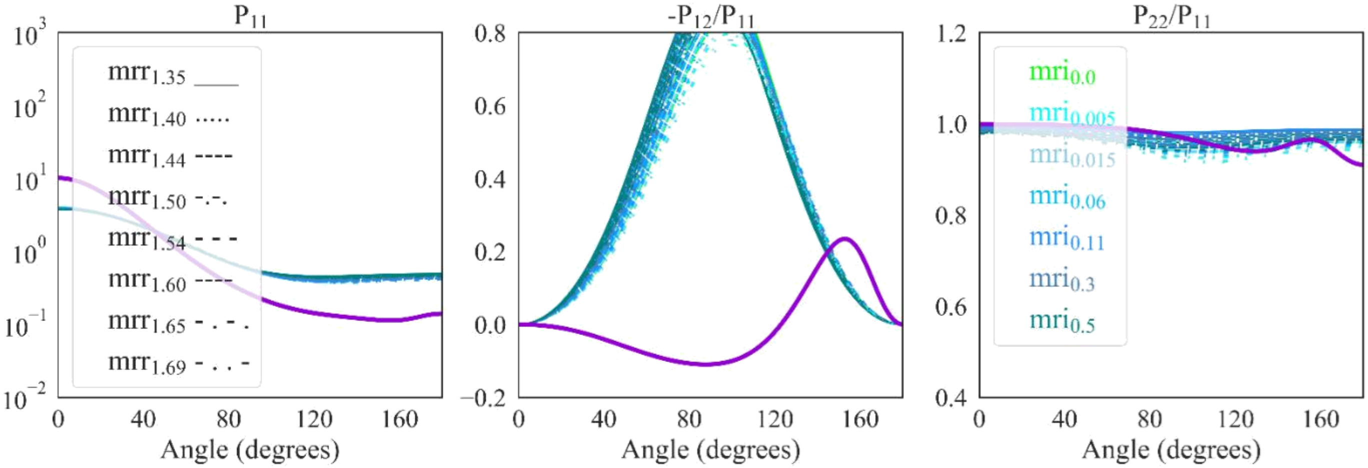

Figure S56. The elements of the scattering matrix at λ = 1020 nm. Left: P11 (phase function), middle: -P12/P11 (degree of linear polarization), right: P22/P11. Purple lines in the plots: calculations considering the near-spherical particle properties derived for the stratospheric smoke particles from the Canadian fires, with mean axial ratio ε_s= 1.3, mono-modal, log-normal size distribution with mean geometric radius r_g = 0.25 µm, mean geometric standard deviation σ_g = 0.4, and complex refractive index m = 1.55 – i0.03. Blue lines in the plots: calculations using the AERONET non-spherical model, monomodal, log-normal size distributions with r_g = 0.1 µm and refractive indices of mrr = 1.35, 1.40, 1.44, 1.50, 1.54, 1.60, 1.65, 1.69 for the real part (different line styles in the plot) and mri = 0.0, 0.005, 0.015, 0.06, 0.11, 0.3, 0.5 for the imaginary part (different line colors in the plot).

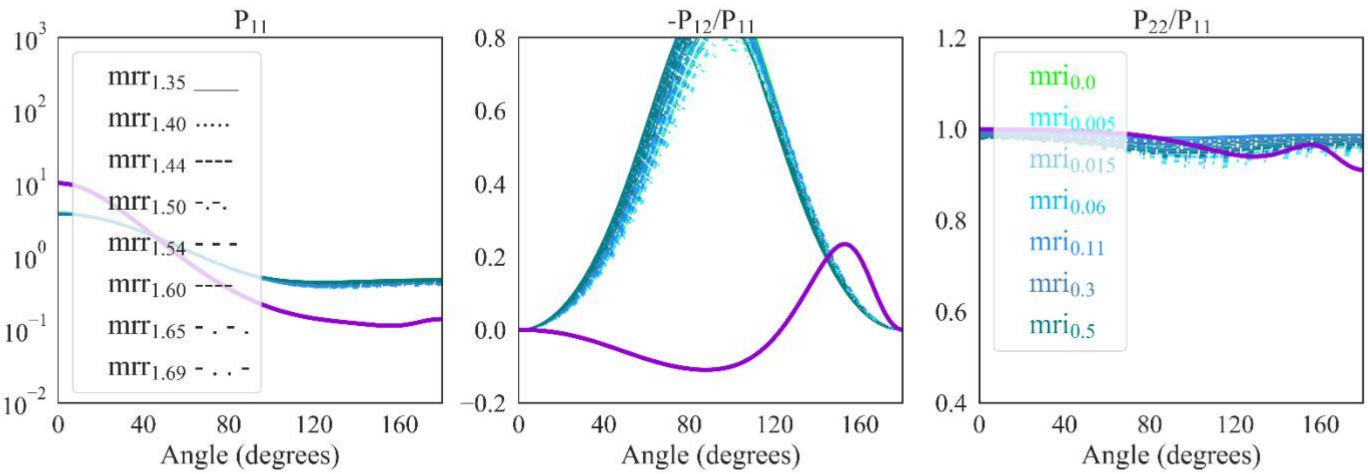

Figure S57. Same as Fig. S56, with the calculations using the AERONET non-spherical model, performed for mono-modal log-normal size distributions with mean geometric radius r_g = 0.15 µm.

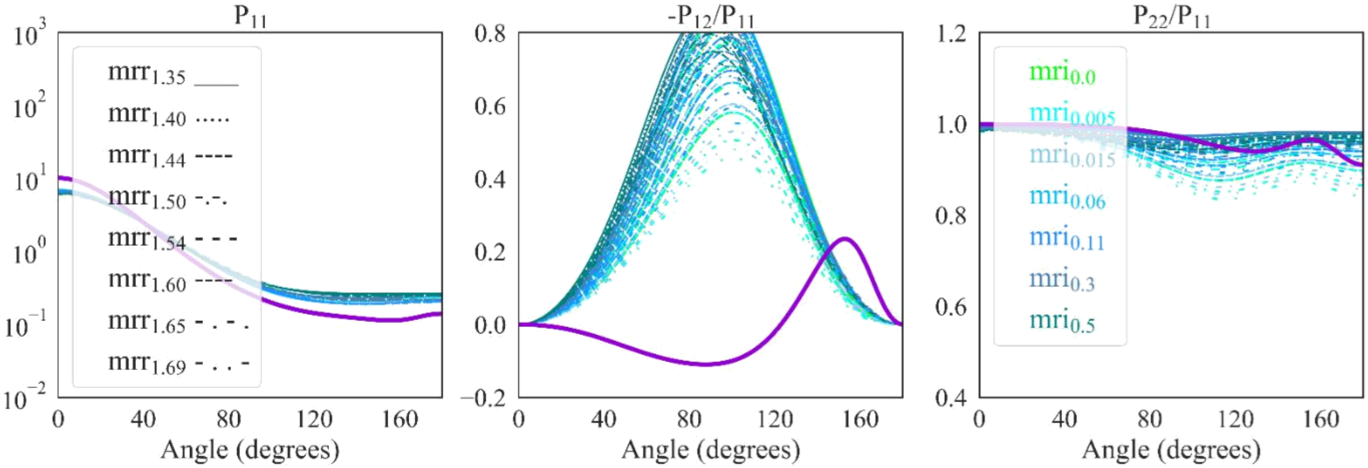

Figure S58. Same as Fig. S56, with the calculations using the AERONET non-spherical model, performed for mono-modal log-normal size distributions with mean geometric radius r_g = 0.2 μm.

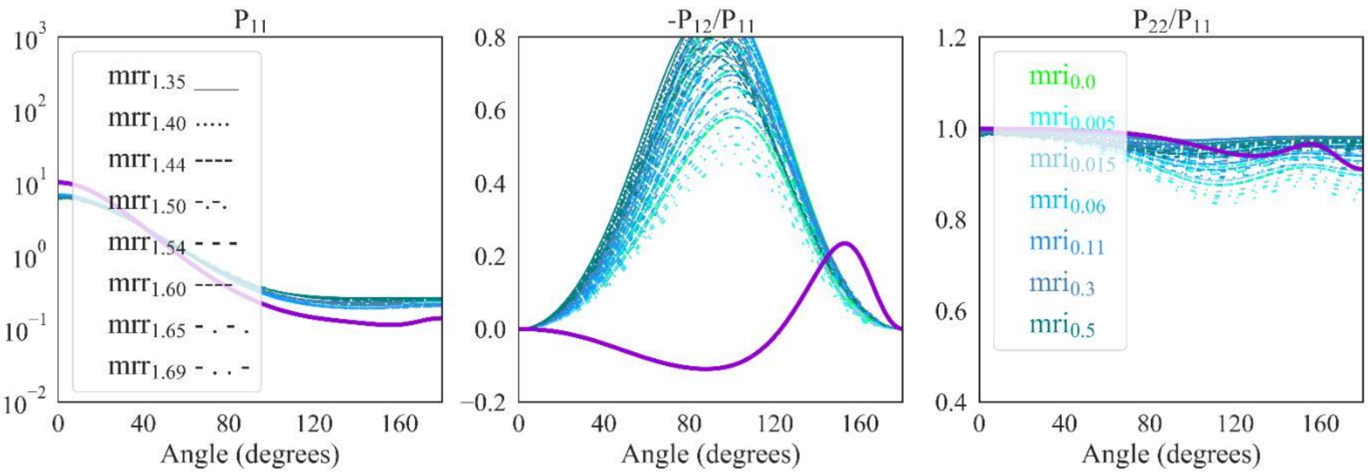

Figure S59. Same as Fig. S56, with the calculations using the AERONET non-spherical model, performed for mono-modal log-normal size distributions with mean geometric radius r_g = 0.25 μm.

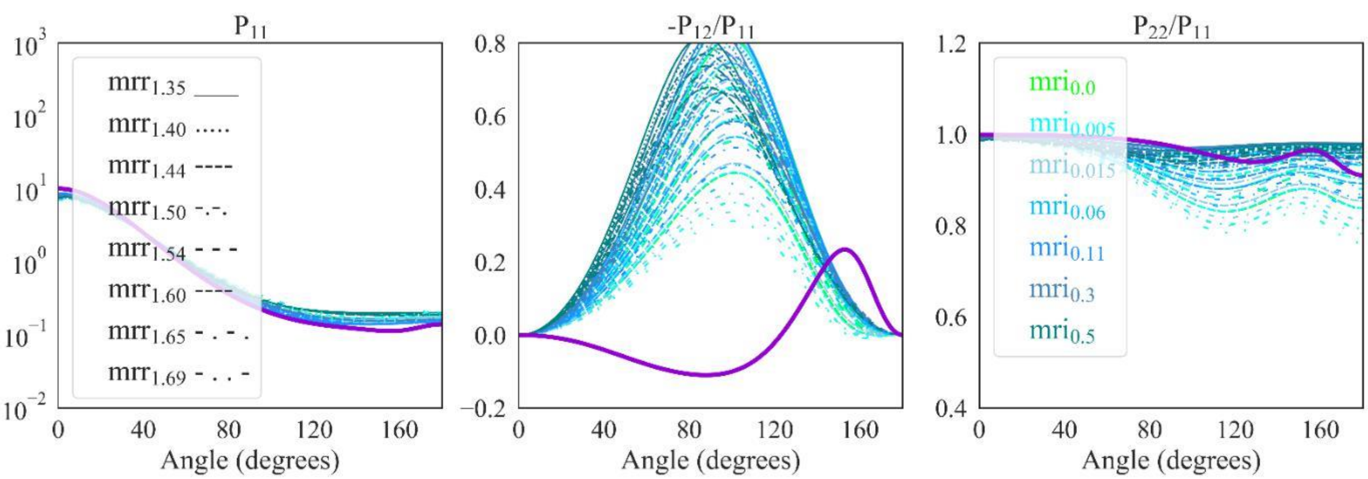

Figure S60. Same as Fig. S56, with the calculations using the AERONET non-spherical model, performed for mono-modal log-normal size distributions with mean geometric radius r_g = 0.3 μm.

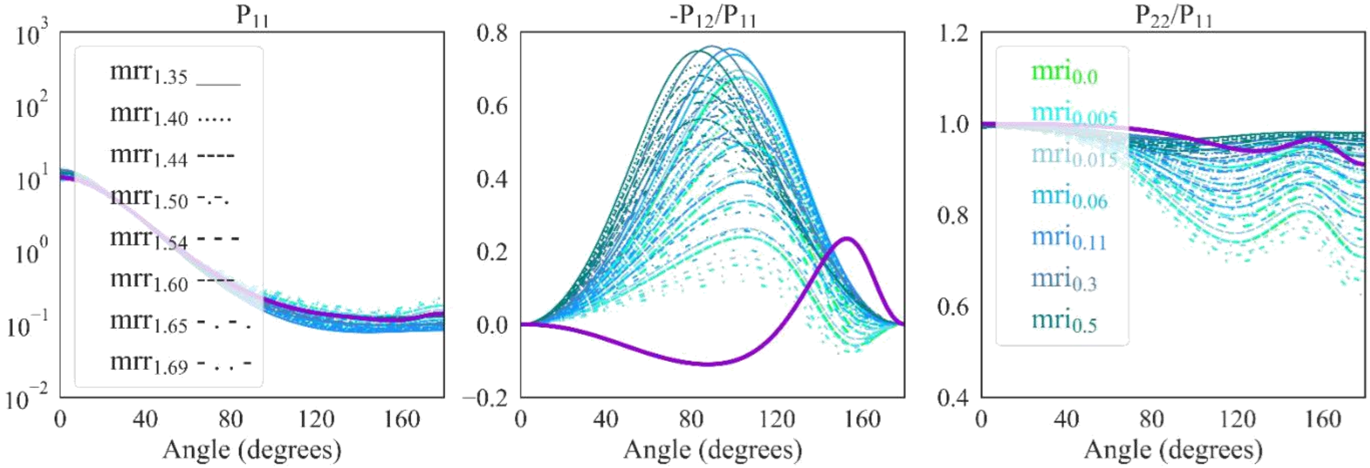

Figure S61. Same as Fig. S56, with the calculations using the AERONET non-spherical model, performed for mono-modal log-normal size distributions with mean geometric radius r_g = 0.4 μm.

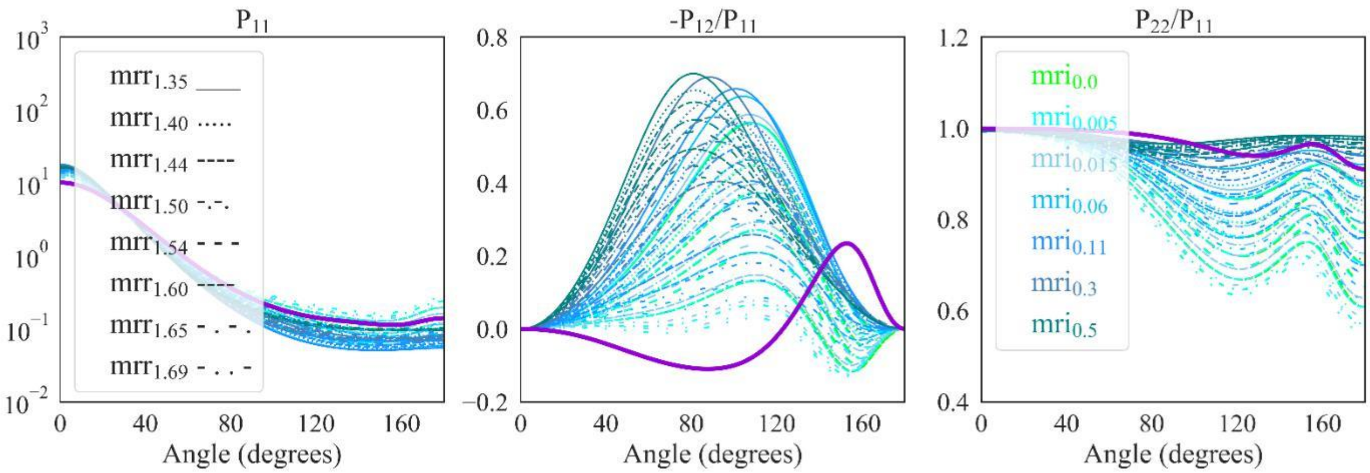

Figure S62. Same as Fig. S56, with the calculations using the AERONET non-spherical model, performed for mono-modal log-normal size distributions with mean geometric radius r_g = 0.5 μm.

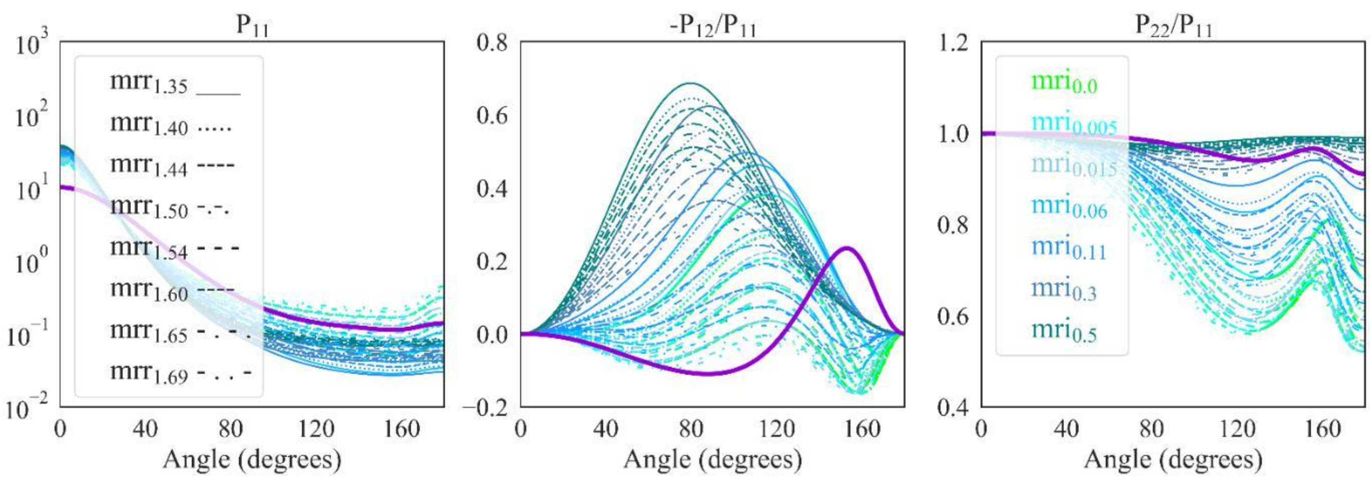

Figure S63. Same as Fig. S56, with the calculations using the AERONET non-spherical model, performed for mono-modal log-normal size distributions with mean geometric radius r_g = 0.8 μm.

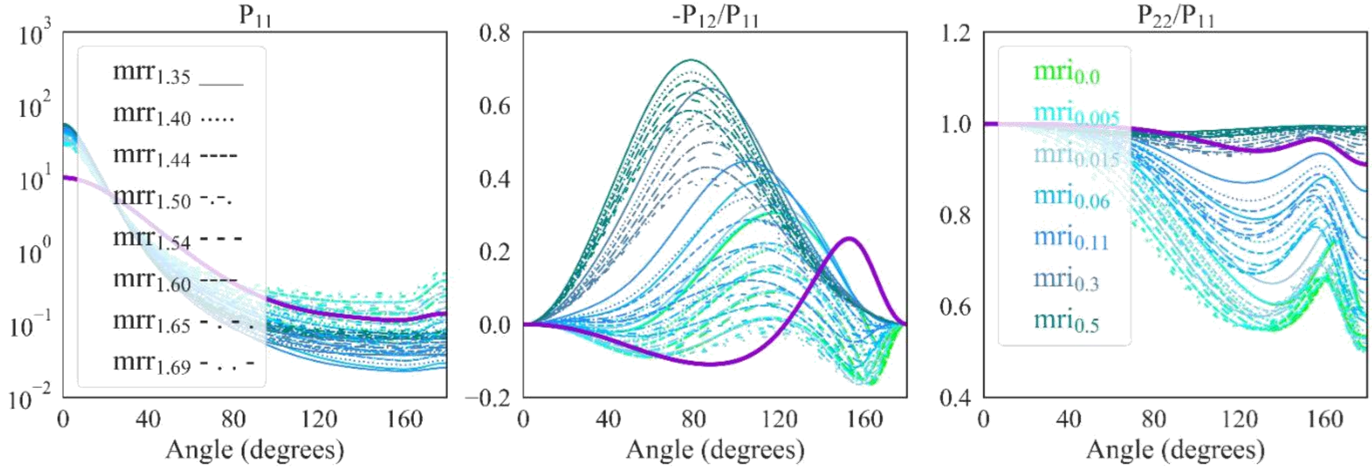

Figure S64. Same as Fig. S56, with the calculations using the AERONET non-spherical model, performed for mono-modal log-normal size distributions with mean geometric radius r_g = 1.0 μm.

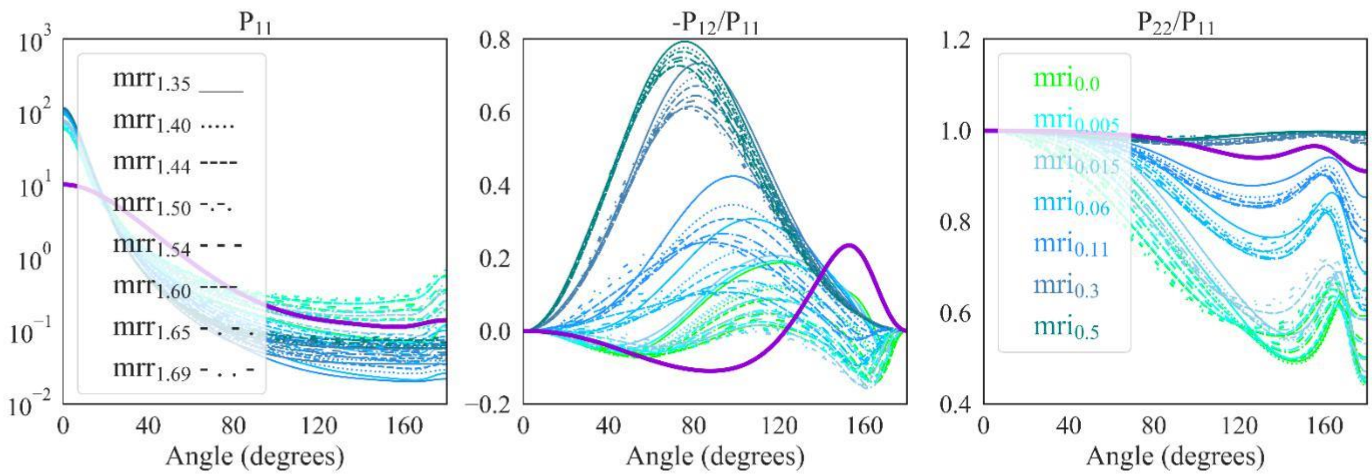

Figure S65. Same as Fig. S56, with the calculations using the AERONET non-spherical model, performed for mono-modal log-normal size distributions with mean geometric radius r_g = 1.5 μm.

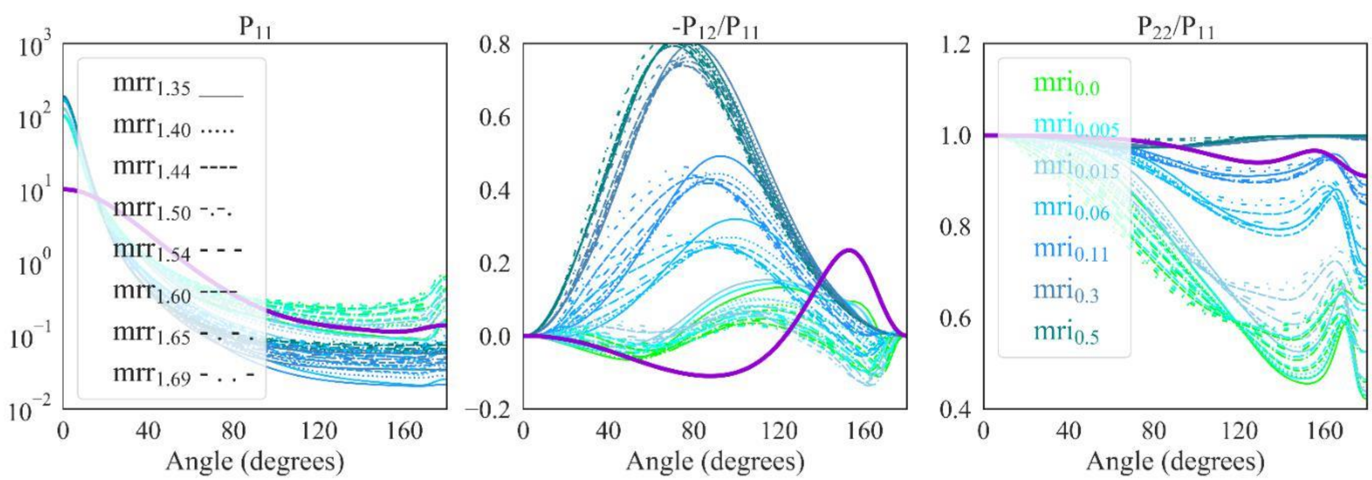

Figure S66. Same as Fig. S56, with the calculations using the AERONET non-spherical model, performed for mono-modal log-normal size distributions with mean geometric radius r_g = 2.0 μm.

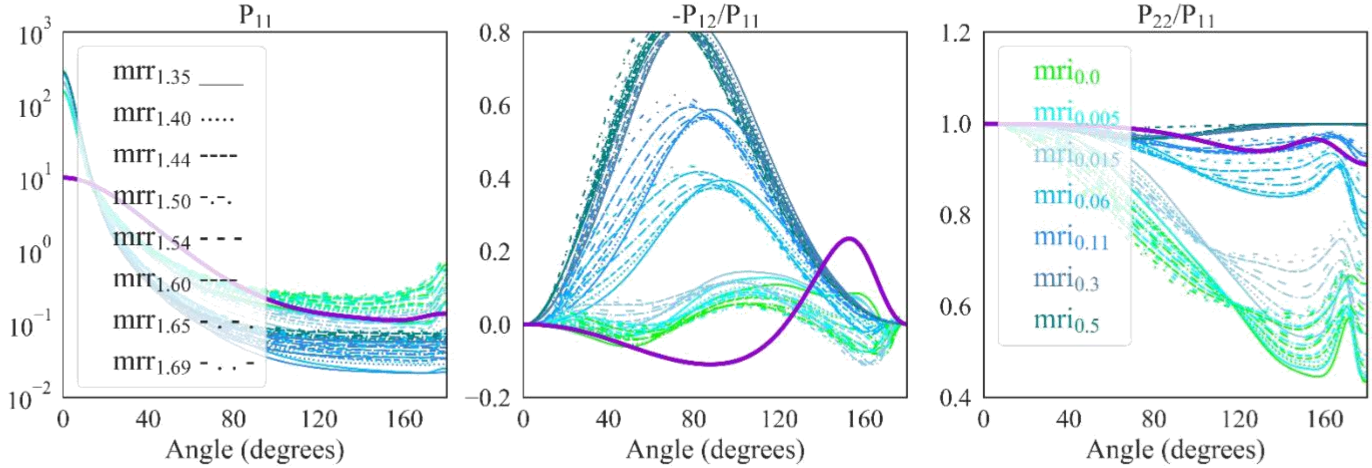

Figure S67. Same as Fig. S56, with the calculations using the AERONET non-spherical model, performed for mono-modal log-normal size distributions with mean geometric radius r_g = 2.5 μm.

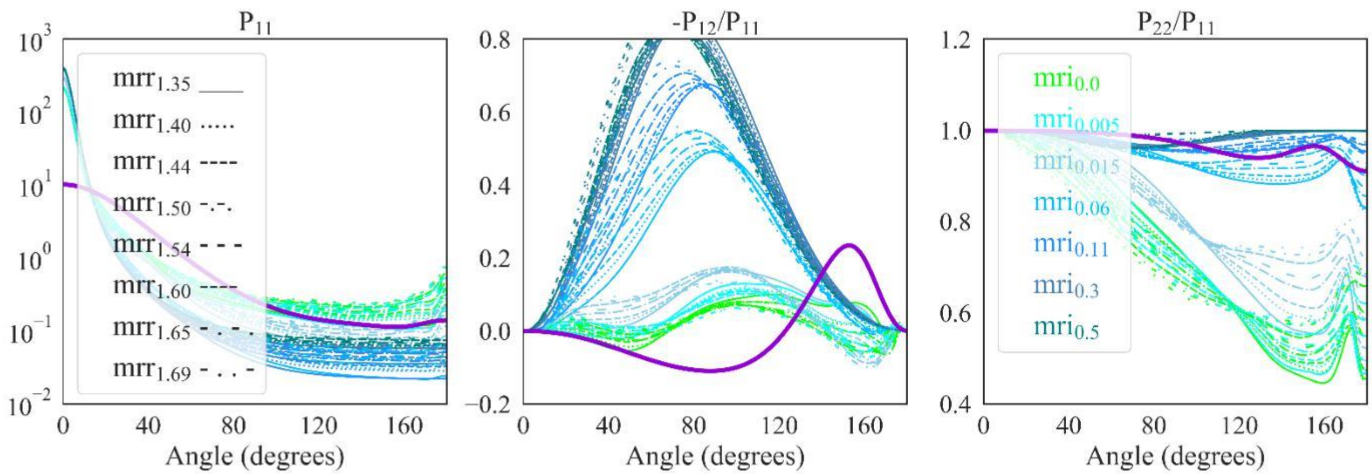

Figure S68. Same as Fig. S56, with the calculations using the AERONET non-spherical model, performed for mono-modal log-normal size distributions with mean geometric radius r_g = 3.0 μm.

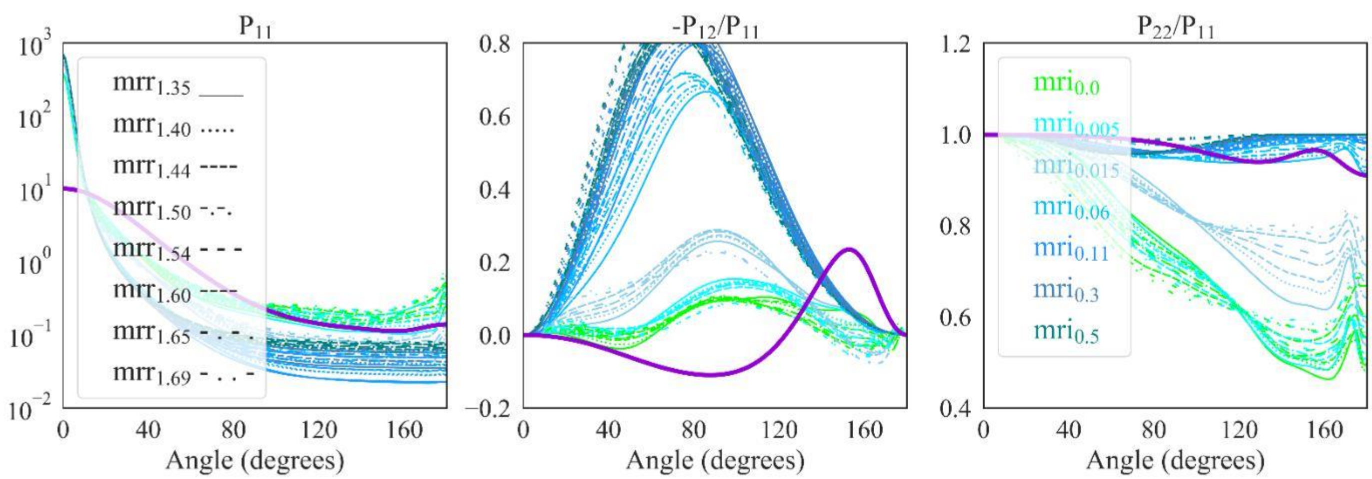

Figure S69. Same as Fig. S56, with the calculations using the AERONET non-spherical model, performed for mono-modal log-normal size distributions with mean geometric radius r_g = 4.0 μm.